4-2011

Scalar EM Beam Propagation in Inhomogeneous Media

John M. Jarem
University of Alabama, Huntsville

Partha P. Banerjee
University of Dayton, pbanerjee1@udayton.edu

2 Scalar EM Beam Propagation in Inhomogeneous Media

2.1 INTRODUCTION

In the previous chapter, we reviewed some of the mathematical preliminaries that will be useful later on in the text. In this chapter, we discuss some of the basic concepts of scalar wave propagation, and discuss an important numerical method, called the beam propagation method (BPM), to study propagation in linear media and in media with induced nonlinearities. Furthermore, we also discuss propagation through induced gratings, both transmission and reflection type, in order to assess energy coupling between participating waves. Finally, we introduce readers to an important characterization method, called the z-scan method, which is often used to determine the focal length of an induced lens.

2.2 TRANSFER FUNCTION FOR PROPAGATION

For simplicity, we consider the *scalar wave equation*

$$\frac{\partial^2 E}{\partial t^2} - v^2 \nabla^2 E = 0 \tag{2.1}$$

and substitute

$$E(x,y,z,t) = \mathrm{Re}\{E_e(x,y,z)\exp[j(\omega_0 t - k_0 z)]\} \tag{2.2}$$

with $\omega_0/k_0 = v$. The quantity E_e is related to the phasor E_p according to

$$E_p(x,y,z) = E_e(x,y,z)\exp(-jk_0 z) \tag{2.3}$$

and we will use one or the other notation according to convenience. Substituting Equation 2.2 into Equation 2.1 and assuming that E_e is a slowly varying function of z (the direction of propagation) in the sense that $\left|\partial^2 E_e/\partial z^2\right| \Big/ \left|\partial E_e/\partial z\right| \ll k_0$, we obtain the paraxial wave equation [1]

$$2jk_0 \frac{\partial E_e}{\partial z} = \nabla_\perp^2 E_e \tag{2.4}$$

where $\nabla_\perp^2$ denotes the transverse Laplacian. Equation 2.4 describes the propagation of the envelope $E_e(x,y,z)$ starting from the initial profile $E_e\big|_{z=0} = E_{e0}(x,y)$.

Equation 2.4 can be solved readily using Fourier transform techniques. Assuming E_e to be Fourier transformable, we can employ the definition of the Fourier transform as in Equation 1.15

$$\tilde{E}_e(k_x,k_y;z) = \Im_{x,y}\{E_e(x,y,z)\} = \int_{-\infty}^{\infty} E_e(x,y,z)\exp(jk_x x + jk_y y)dx\,dy \tag{2.5}$$

and its properties to transform Equation 2.4 into the ordinary differential equation (ODE)

$$\frac{d\tilde{E}_e}{dz} = \frac{j}{2k_0}(k_x^2 + k_y^2)\tilde{E}_e \tag{2.6}$$

We can easily solve Equation 2.6 to give

$$\tilde{E}_e(k_x, k_y; z) = \tilde{E}_{e0}(k_x, k_y)\exp\left\{\frac{j(k_x^2 + k_y^2)z}{2k_0}\right\} \tag{2.7}$$

where $\tilde{E}_{e0}(k_x, k_y)$ is the Fourier transform of $E_{e0}(x, y)$. We can interpret Equation 2.7 in the following way: Consider a linear system with an input spectrum of $\tilde{E}_{e0}(k_x, k_y)$ at $z = 0$ where the output spectrum at z is given by $\tilde{E}_e(k_x, k_y; z)$. The spatial frequency response of the system, which we will call the *paraxial transfer function for propagation* is then given by

$$\frac{\tilde{E}_e}{\tilde{E}_{e0}} = H(k_x, k_y; z) = \exp\left\{\frac{j(k_x^2 + k_y^2)z}{2k_0}\right\} \tag{2.8}$$

As we will show later, in the split-step BPM, we model propagational diffraction by means of the transfer function for propagation derived above. For more exact calculations, the nonparaxial transfer function can be used. This may be derived starting from the nonparaxial wave equation, but will not be presented here for the sake of simplicity.

Incidentally, the inverse Fourier transform of the transfer function for propagation yields the *impulse response for propagation*. Starting from the paraxial transfer function for propagation which resembles a complex Gaussian, the inverse Fourier transform is a complex Gaussian as well, and has the form

$$h(x, y, z) = \frac{jk_0}{2\pi z}\exp\left[\frac{-j(x^2 + y^2)k_0}{2z}\right] \tag{2.9}$$

This, when convolved with the initial beam profile, yields the profile of the diffracted beam in the spatial domain directly. This convolution integral is in fact the Fresnel diffraction formula.

2.3 SPLIT-STEP BEAM PROPAGATION METHOD

If we wish to consider propagation in a material where the propagation constant or equivalently the refractive index is a function of position, either due to profiling of the material itself (such as a graded index fiber or a grating) or due to induced effects such as third order nonlinearities, the paraxial wave equation changes to

$$\frac{\partial E_e}{\partial z} = \frac{1}{2jk_0}\nabla_\perp^2 E_e - j\Delta n k_0 E_e \tag{2.10}$$

The quantity Δn is the change in the refractive index over the ambient refractive index $n_0 = c/v$, where c is the velocity of light in vacuum. Equation 2.10 is a modification of Equation 2.4 and can be derived from the scalar wave equation when the propagation constant or equivalently the velocity of the wave is a function of (x, y, z) explicitly as in gratings or fibers, or implicitly such as through the intensity dependent refractive index. An alternative, though heuristic, way to justify the presence of the additional term on the RHS of Equation 2.10 is to note that in the absence of diffraction (the first term on the RHS), the solution of the equation is of the form $E_e \propto \exp[-j\Delta n k_0 z]$, which explicitly shows the additional phase change due to propagation in the perturbed refractive index.

The paraxial propagation equation (2.10) is a partial differential equation (PDE) that does not always lend itself to analytical solutions, except for some very special cases involving special spatial variations of Δn, or when as in nonlinear optics, one looks for particular soliton solution of the resulting nonlinear PDE using exact integration or inverse scattering methods. Numerical approaches are often sought for to analyze beam (and pulse) propagation in complex systems such as optical fibers, volume diffraction gratings, Kerr and photorefractive (PR) media, etc. A large number of numerical methods can be used for this purpose. The pseudospectral methods are often favored over finite difference methods due to their speed advantage. The split-step BPM is an example of a pseudospectral method.

To understand the philosophy behind the BPM, it is useful to rewrite Equation 2.10 in the form [2,3]

$$\frac{\partial E_e}{\partial z} = (\hat{D} + \hat{S})E_e \tag{2.11}$$

where $\hat{D}$, $\hat{S}$ are a linear differential operator and a space dependent or nonlinear operator respectively (see, for instance, the structure of Equation 2.10). Thus, in general, the solution of Equation 2.11 can be symbolically written as

$$E_e(x, y, z + \Delta z) = \exp[(\hat{D} + \hat{S})\Delta z]E_e(x, y, z) \tag{2.12}$$

if $\hat{D}$, $\hat{S}$ are assumed to be z-independent. Now for two noncommuting operators $\hat{D}$, $\hat{S}$,

$$\exp(\hat{D}\Delta z)\exp(\hat{S}\Delta z) = \exp\left(\hat{D}\Delta z + \hat{S}\Delta z + \left(\frac{1}{2}\right)[\hat{D}, \hat{S}](\Delta z)^2 + \cdots\right) \tag{2.13}$$

according to the Baker–Hausdorff formula [2], where $[\hat{D}, \hat{S}]$ represents the commutation of $\hat{D}$, $\hat{S}$. Thus, up to second order in Δz,

$$\exp(\hat{D}\Delta z + \hat{S}\Delta z) \cong \exp(\hat{D}\Delta z)\exp(\hat{S}\Delta z) \tag{2.14}$$

which implies that in Equation 2.13 the diffraction and the inhomogeneous operators can be treated independent of each other.

The action of the first operator on the RHS of Equation 2.14 is better understood in the spectral domain. Note that this is the propagation operator that takes into account the effect of diffraction between planes z and $z + \Delta z$. Propagation is readily handled in the spectral or spatial frequency domain using the transfer function for propagation written in Equation 2.8 with z replaced by Δz. The second operator describes the effect of propagation in the absence of diffraction and in the presence of medium inhomogeneities, either intrinsic or induced, and is incorporated in the spatial

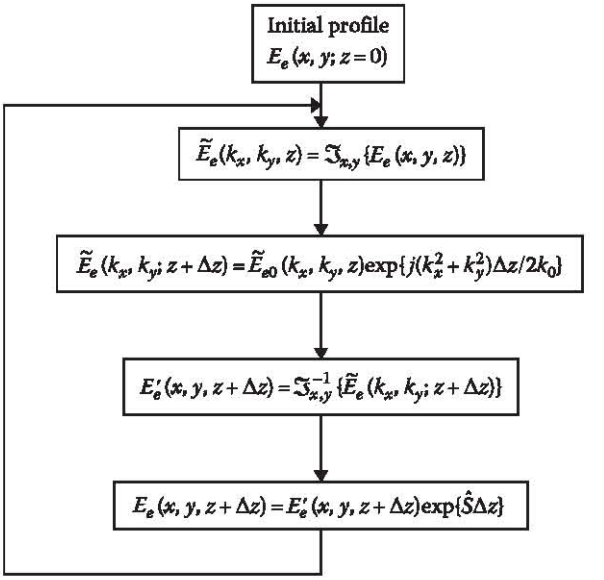

FIGURE 2.1 Flow diagram for the BPM split-step method.

domain. A schematic block diagram of the BPM method in its simplest form is shown in Figure 2.1. There are other modifications to the simple scheme, viz., the symmetrized split-step Fourier method, and the leap-frog techniques; these are discussed in detail elsewhere [2].

2.4 BEAM PROPAGATION IN LINEAR MEDIA

In this section, we will illustrate various cases where the BPM can be used to analyze propagation in inhomogeneous media. While most of the examples will be connected with beam propagation, we must point out to readers that the method can be used to analyze pulse propagation as well, simply by replacing z in Equation 2.11 with t (time), and making the linear spatial transverse differential operator a similar differential operator in z. With this modification, Equation 2.11 can model the propagation of one dimensional longitudinal pulse through an optical fiber with arbitrary group velocity dispersion. For details, we refer the readers to Agrawal [2].

2.4.1 Linear Free-Space Beam Propagation

The propagation of Gaussian beams through free space can be readily analyzed analytically using the transfer function of propagation. For a traditional scalar (or x- or y-polarized) Gaussian beam, $E_e(x, y; z = 0)$ is a Gaussian function of the form

$$E_e(x, y; 0) = E_0 \exp[-\alpha(x^2 + y^2)] \tag{2.15}$$

with a Fourier transform

$$\tilde{E}_e(k_x, k_y; 0) = E_0\left(\frac{\pi}{\alpha}\right)\exp\left[-\frac{(k_x^2 + k_y^2)}{4\alpha}\right] \tag{2.16}$$

where α may be complex. Hence, using Equation 2.8,

$$\begin{aligned}\tilde{E}_e(k_x,k_y;z) &= \tilde{E}_e(k_x,k_y;0)H(k_x,k_y;z)\\ &= E_0\left(\frac{\pi}{\alpha}\right)\exp\left[-\frac{(k_x^2+k_y^2)}{4\alpha}\right]\exp\left[\frac{j(k_x^2+k_y^2)z}{2k_0}\right]\\ &= E_0\left(\frac{\pi}{\alpha}\right)\exp\left[\frac{j(k_x^2+k_y^2)q}{2k_0}\right]\end{aligned} \tag{2.17}$$

whose inverse transform is a Gaussian in transverse spatial dimensions:

$$E_e(x,y;z) = \frac{jk_0}{2\pi q}E_0\left(\frac{\pi}{\alpha}\right)\exp\left[-\frac{jk_0(x^2+y^2)}{2q}\right] \tag{2.18}$$

Equation 2.17 defines the well-known q-parameter of the Gaussian beam:

$$q = z + \frac{jk_0}{2\alpha} \tag{2.19}$$

If the initial Gaussian beam has waist w_0 and plane wavefronts, $\alpha = 1/w_0^2$ and $q = z + jz_R$, where $z_R = k_0w_0^2/2$ is commonly referred to as the *Rayleigh range* of the Gaussian beam. Upon simplifying Equation 2.18 using Equation 2.19, we get the standard expression for the diffracted Gaussian beam profile as

$$E_e(x,y;z) = \frac{w_0}{w(z)}E_0\exp\left[-\frac{(x^2+y^2)}{w^2(z)}\right]\exp\left[-\frac{jk_0(x^2+y^2)}{2R(z)}\right]e^{-j\phi(z)} \tag{2.20}$$

where

$$w^2(z) = w_0^2\left[1+\left(\frac{z}{z_R}\right)^2\right],\quad R(z) = \frac{(z^2+z_R^2)}{z},\quad \phi(z) = -\tan^{-1}\left(\frac{z}{z_R}\right) \tag{2.21}$$

Incidentally, if a Gaussian beam with initially plane wavefronts passes through a (thin) lens of focal length f, the latter introduces a quadratic phase curvature which can be accommodated by multiplying the initial Gaussian with a complex exponential $\exp[jk_0(x^2+y^2)/2f]$. In this case, the scalar optical field immediately behind the lens ($z = 0^+$) can be written in the form as in Equation 2.15 above, but where α is redefined as

$$\alpha = \frac{1}{w_0^2} - \frac{jk_0}{2f} = \left(\frac{1}{w_0^2}\right)\left(\frac{1-jz_R}{f}\right) \tag{2.22}$$

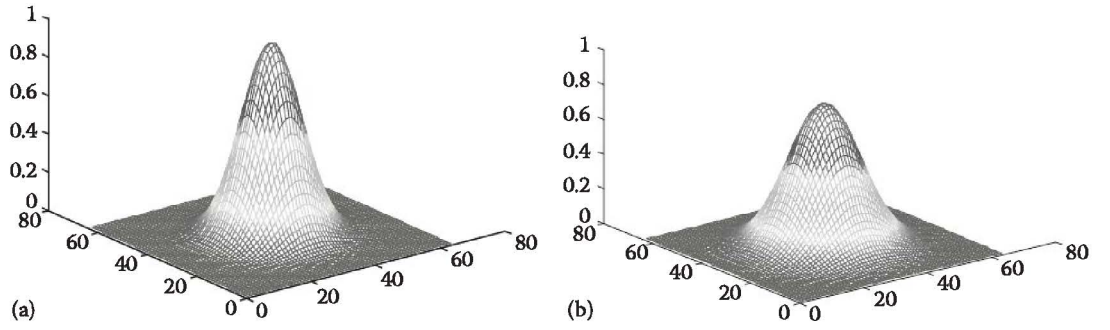

FIGURE 2.2 Diffraction of a Gaussian beam during free-space propagation: (a) profile at $z = 0$ (plane wavefronts assumed) and (b) profile at $z = z_R$, where z_R is the Rayleigh range of the original Gaussian beam.

The paraxial propagation of a Gaussian beam through an optical system involving translation and lensing can be equivalently studied in terms of the variation of the q-parameter. For instance, due to propagation in air through a distance z alone, the change in the q-parameter can be readily found from Equation 2.17 as

$$q_{new} = q_{old} + z \tag{2.23a}$$

On the other hand, if a Gaussian beam is incident on a lens of focal length f, the change in the q-parameter can be readily found from Equation 2.18 and the phase transformation by the lens given above as

$$\frac{1}{q_{new}} = \frac{1}{q_{old}} - \frac{1}{f} \tag{2.23b}$$

Equation 2.23a and b will be later used to analyze propagation of Gaussian beams through media which have a distributed lensing effect, such as a nonlinear medium.

We now demonstrate the application of BPM to Gaussian beam propagation through free space. In this case, the inhomogeneous operator is zero, and propagation from a plane $z = 0$ to arbitrary z can indeed be performed in one step in this case. However, in the example we provide, we use the split-step method to convince readers that the result is identical to what one would get if the propagation was covered in one step. In Figure 2.2, we show the profile of a diffracted Gaussian beam after propagation through free space, and the results agree with the physical intuition of increased width and decreased on-axis amplitude during propagation as well as the analytical results in Equations 2.20 and 2.21.

2.4.2 Propagation of Gaussian Beam through Graded Index Medium

A *graded index medium* has a refractive index variation of the form

$$n = n_0 + n^{(2)}(x^2 + y^2) \tag{2.24}$$

where n_0 denotes the intrinsic refractive index of the medium, and $n^{(2)}$ is a measure of the gradation in the refractive index.

In this case, the operator $\hat{S}$ becomes

$$\hat{S} = -jk_0 n^{(2)}(x^2 + y^2) \tag{2.25}$$

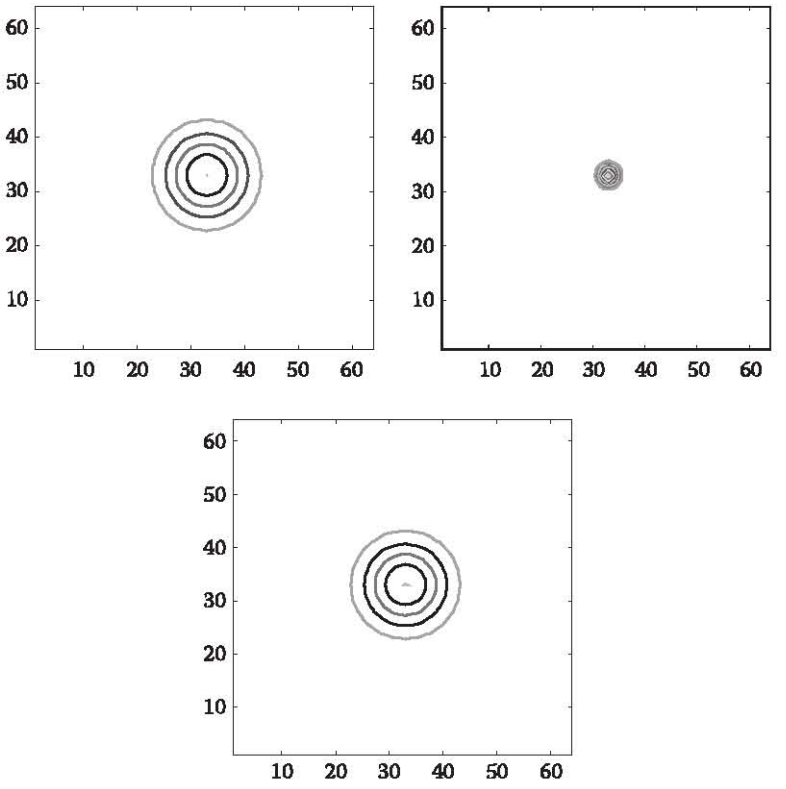

FIGURE 2.3 Contour plots showing periodic focusing of an initial Gaussian profile.

Propagation of a Gaussian beam in a medium with a graded index profile is shown in Figure 2.3. The contour plots show the initial (Gaussian) beam profile, the beam profile where the initial Gaussian attains its minimum waist during propagation before returning back to its original shape again, due to periodic focusing by the graded index distribution. Note that there exists a specific eigenmode (a Gaussian of a specific width, related to the refractive index gradient) for which the beam propagates through the material without a change in shape as a result of a balance between the diffraction of the beam and the guiding due to the parabolic gradient index profile. The contour plot of such a beam is shown in Figure 2.4. Analytical expressions for the Gaussian beam

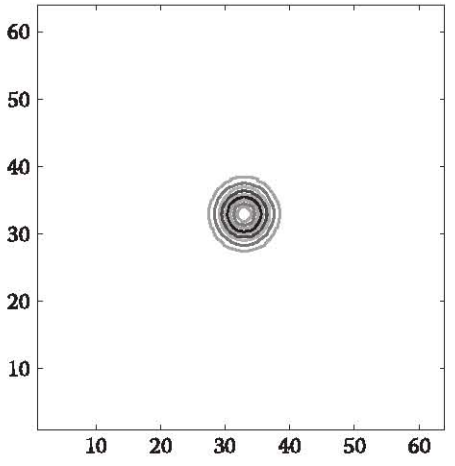

FIGURE 2.4 Fundamental mode in a graded index fiber.

during propagation through a graded index medium and for the eigenmode can be derived using the q-parameter of the Gaussian beam and the ABCD laws of q-transformation, but will not be pursued here for the sake of brevity.

2.5 BEAM PROPAGATION THROUGH DIFFRACTION GRATINGS: ACOUSTOOPTIC DIFFRACTION

The beam propagation algorithm has been applied to the propagation of a beam through a grating, and can be also used to analyze the case where the grating is a sound field. In what follows, we give an example of the use of BPM to analyze diffraction of light by an acoustooptic cell in which a traveling wave of sound causes a change in the refractive index using a *modified* split-step technique. The modification consists of the fact that the inhomogeneity due to the refractive index grating is accomodated for in the spatial frequency domain as well.

The perturbation Δn in the case of sound induced gratings is a function of time and space:

$$\Delta n(x,z,t) = Cs(x,z,t) \tag{2.26}$$

where C is an interaction constant (for details, see Korpel [4]) and $s(x, z, t)$ is the real sound amplitude given by,

$$s(x,z,t) = \frac{1}{2}[S_e(x,z)\exp(-jKx)\exp(j\Omega t) + \text{c.c.}] \tag{2.27}$$

where S_e is the complex amplitude of the sound field that interacts with the light beam and is traveling in the x direction, and c.c. denotes the complex conjugate.

The quantities K and Ω are the propagation constant and the angular frequency, respectively, of the sound field. Following Refs. [4,5], a snapshot of the sound field is used at $t = 0$, so that using 2.26 and 2.27,

$$\begin{aligned}\exp(\hat{S}\Delta z) &= \exp(-jk_0\Delta n\Delta z) \approx 1 - jk_0\Delta n\Delta z \\ &= 1 - \left(\frac{1}{2}\right) jk_0\Delta z C\,[S_e(x,z)\exp(-jKx) + S_e{}^*(x,z)\exp(+jKx)]\end{aligned} \tag{2.28}$$

In the modified split-step technique, we take the Fourier transform of the above operator operating on the optical field $E_e(x,z)$, taking care to note from the property of Fourier transforms that

$$\Im_x[f(x)\exp(\pm jKx)] = \tilde{f}(k_x \pm K) \tag{2.29}$$

The main propagation loop of the algorithm is modified from Figure 2.1 and is shown in Figure 2.5. The boxes marked "Shift $\pm K$" are used to facilitate the operation shown in 229 in the spatial frequency domain.

Figure 2.6 shows problem geometry of a Gaussian beam incident nominally at Bragg angle on a sound column of width $z = L$. The simulated evolution of the Gaussian beam is shown in Figure 2.7. The peak phase delay α of the light traveling through the acoustooptic cell is taken equal to π, and the *Klein–Cook parameter* $Q = K^2L/k_0 = 13.1$. We would like to point out that the same answers could be derived by using the transfer function for acoustooptic interaction, as given in Refs. [4,6].

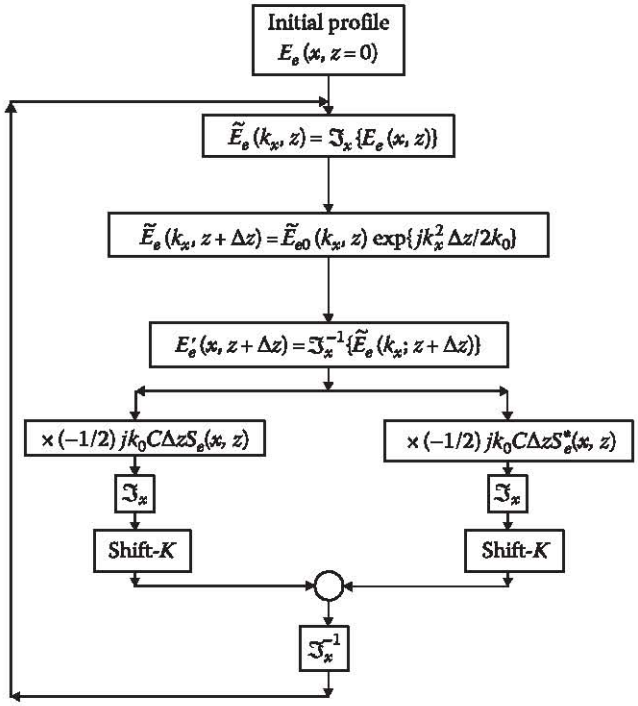

FIGURE 2.5 Flow diagram for the modified split-step technique to analyze acoustooptic interaction.

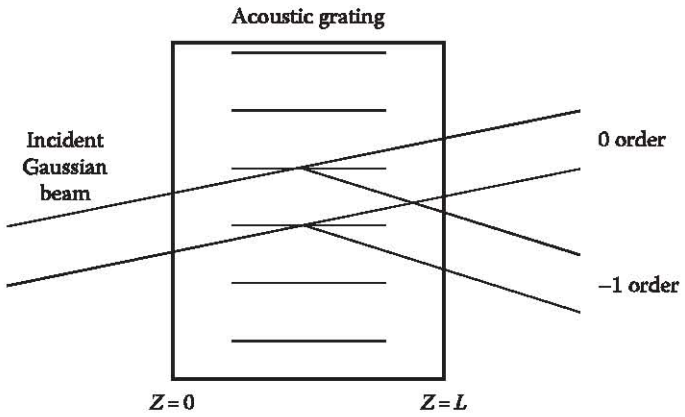

FIGURE 2.6 Geometry of acoustooptic interaction with a Gaussian beam at nominal Bragg incidence.

2.6 BEAM PROPAGATION IN KERR-TYPE NONLINEAR MEDIA

2.6.1 Nonlinear Schrodinger Equation

The nonlinear propagation of beams through a cubically nonlinear material is modeled by the nonlinear PDE also called the *nonlinear Schrodinger* (NLS) equation [7]

$$2jk_0\frac{\partial E_e}{\partial z} = \nabla_\perp^2 E_e + 2n_2k_0^2\left|E_e\right|^2 E_e \tag{2.30}$$

where n_2 is the *nonlinear refractive index coefficient* defined by the functional dependence of the total refractive index n on the intensity [7]:

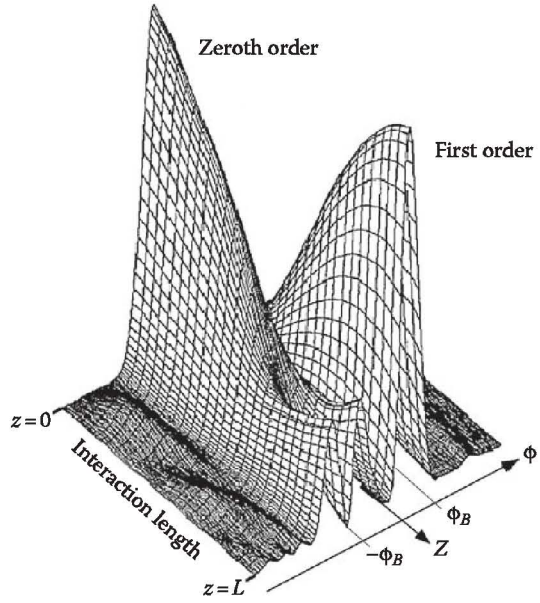

FIGURE 2.7 Simulation plot of the intensity of the angular spectrum of the total field at different positions along interaction length. (From Venzke, C. et al., *Appl. Opt.*, 31, 656, 1992. With permission.)

$$n = n_0 + \delta n\left(\left|E_e\right|^2\right) = n_0 + n_2\left|E_e\right|^2 \tag{2.31}$$

In writing (2.30), we have taken the linear refractive index n_0 equal to unity for the sake of simplicity. For a medium with $n_2 > 0$, one can observe *self-focusing* of a Gaussian beam traveling through a medium, while *self-defocusing* is observed for a medium with $n_2 < 0$. The physical reasoning behind self-focusing is as follows. The Gaussian beam induces a positive lens in the nonlinear material for $n_2 > 0$ due to the fact that where the beam intensity is high (e.g., on-axis), the induced refractive index is higher as well, amounting to larger slowing down of the wavefronts. The wavefronts are therefore bent similar to the action of a positive lens, resulting in initial focusing of the beam. This process continues till the beam width is small enough for the diffraction effects to take over, leading to an increase in the beam width. The converse is true for the case of $n_2 < 0$. In this case, the beam spreads more than in the linear diffraction limited case. A stable nonspreading solution in one transverse dimension can be analytically found from the NLS equation for $n_2 > 0$ and has the form

$$\left|E_e(x;z)\right| = \left(\frac{8\kappa}{n_2 k_0}\right)^{1/2} \operatorname{sech}\frac{x}{(2\kappa k_0)^{1/2}} \tag{2.32}$$

where κ is a free parameter. The phase of E_e in the nonspreading solution is linearly proportional to the propagation distance z.

As discussed above, self-focusing results in increase in the on-axis intensity and the narrowing of the beam width. For powers above a certain critical power P_c [7,8], the beam may theoretically collapse with an intensity so high that it can either cause breakdown in the material, triggering some other physical effects, such as saturation of the index of refraction or failure of the assumptions about slowly varying amplitude and paraxial approximation. Zakharov and Shabat [9] have pointed out that if the nonlinearity is strong enough, this results in higher index of refraction toward the center of the beam and on-axis rays undergo total internal reflection and are thereby trapped. As shown above, nonlinearity can balance diffraction of a beam in one dimension, resulting in the formation of first order spatial solitons, see Equation 2.32. Also, if the nonlinear effect is higher

than diffraction, periodic focusing occurs, or may result in higher order solitons. This may not be the case in two or three dimensions where spatial collapse may occur.

In normalized form, and assuming $n_2 > 0$, the NLS equation in Equation 2.30 can be rewritten as

$$j\frac{\partial \tilde{u}_e}{\partial z} + \nabla_\perp^2 \tilde{u}_e + \left|\tilde{u}_e^2\right| \tilde{u}_e = 0 \tag{2.33}$$

In a system with cylindrical symmetry, Equation 2.33 becomes

$$j\frac{\partial \tilde{u}_e}{\partial z} + \frac{1}{r}\frac{\partial \tilde{u}_e}{\partial r} + \frac{\partial^2 \tilde{u}_e}{\partial r^2} + \left|\tilde{u}_e^2\right| \tilde{u}_e = 0 \tag{2.34}$$

The NLS equation as written in Equation 2.33 can also be modified to model pulse propagation through a nonlinear fiber and in the presence of group velocity dispersion. This is possible due to the fact that the interchange $x \rightarrow t$ in the NLS equation (2.33) with a suitable coefficient in front of the second order derivative term, signifying (anomalous) material dispersion and subsequent renormalization transforms the equation to one that can model the propagation of pulses in time τ along a fiber [2]:

$$j\frac{\partial \tilde{u}_e}{\partial z} + \frac{1}{2}\frac{\partial^2 \tilde{u}_e}{\partial \tau^2} + \gamma' \left|\tilde{u}_e\right|^2 \tilde{u}_e = 0 \tag{2.35}$$

Analogous to Equation 2.32, the *first order soliton* solution of (2.35) can be expressed as

$$\left|\tilde{u}_e(\tau; z)\right| = K \operatorname{sech}\left(K\sqrt{\gamma'}\tau\right) \tag{2.36}$$

where K is a free parameter. This profile is called a *temporal soliton* and can be regarded as a nonlinear eigenmode of the NLS system. The propagation of an initial profile $\tilde{u}_e(\tau; z = 0) = \operatorname{sech}\left(\sqrt{\gamma'}\tau\right)$ with $\gamma' = 1$ using the BPM to model the NLS equation as in Equation 2.35 is shown in Figure 2.8. The linear term in Equation 2.35 can be handled in the temporal frequency domain by using Fourier transforms, similar to the case of propagational diffraction. Note that the nonlinear operator is

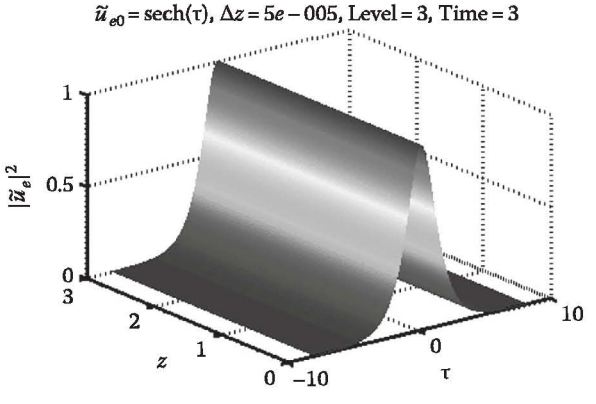

FIGURE 2.8 Evolution of a first order 1-D soliton. (From Nehmetallah, G. and Banerjee, P.P., *Nonlinear Optics and Applications*, H.A. Abdeldayem and D.O. Frazier, eds., Research Signpost, Trivandrum, India, 2007. With permission.)

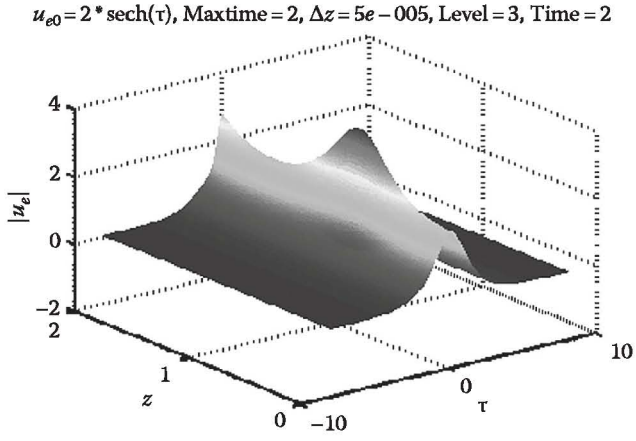

FIGURE 2.9 Evolution of a second order 1-D soliton. (From Nehmetallah, G. and Banerjee, P.P., *Nonlinear Optics and Applications*, H.A. Abdeldayem and D.O. Frazier, eds., Research Signpost, Trivandrum, India, 2007. With permission.)

$\exp\{\hat{S}\Delta z\} = \exp -j\gamma' |\tilde{u}_e|^2 \Delta z$. As expected, the "pulse" remains unchanged with propagation. A similar result is obtained if we program the propagation of an initial beam profile and use Equation 2.30 in one transverse dimension (x). The result is a *spatial soliton*.

The *second order soliton* input $\tilde{u}_e(\tau, 0) = 2\,\mathrm{sech}(\tau)$ and its evolution in time is shown in Figure 2.9. The split-step technique has also been applied to analyze propagation of profiles in two transverse dimensions [11], and also to analyze propagation of optical fields that are pulsed in time and have a spatial profile in the transverse dimension [12].

2.6.2 Simulation of Self-Focusing Using Adaptive Fourier and Fourier–Hankel Transform Methods

The NLS equation for beams using the paraxial approximation has been previously derived in Section 2.6.1 as

$$j\frac{\partial \tilde{u}_e}{\partial z} + \nabla_\perp^2 \tilde{u}_e + \left|\tilde{u}_e^2\right| \tilde{u}_e = 0 \tag{2.37}$$

During the last stages of self-focusing, the assumptions about slowly varying amplitude and the paraxial approximation may not be valid for large focusing angles. It has been proposed that there is no singularity if one accounts for nonparaxiality [13]. The paraxial and nonparaxial NLS equations which are classically used to model the self-focusing phenomenon can be written in the general operator form:

$$\frac{\partial \tilde{u}_e}{\partial z} - j\varepsilon \frac{\partial^2 \tilde{u}_e}{\partial z^2} = jL_r\tilde{u}_e + jN_{nl}(\tilde{u}_e)\tilde{u}_e, \quad \vec{r} \in \Re^D, \quad z \geq 0; \quad \tilde{u}_e(r, z = 0) = \tilde{u}_{e0}(r) \tag{2.38}$$

where D is the transverse dimension in space. The parameter $\varepsilon = (\lambda/4\pi r_0)^2$, where r_0 is the initial beam radius is often referred to as the *nonparaxiality parameter*. Also, $L_r\tilde{u}_e = \nabla_\perp^2 \tilde{u}_e$, $N_{nl}(\tilde{u}_e) = |\tilde{u}_e|^{2\sigma}$. For most cases, $\sigma = 1$ and hence $N_{nl}(\tilde{u}_e) = |\tilde{u}_e|^2$. The nonlinear operator $N_{nl}(\tilde{u}_e)$ may be also conveniently modified to reflect any saturation in the change of refractive index:

$$\delta n\left(|\tilde{u}_e|^2\right) = n_2 |\tilde{u}_e|^2 + n_4 |\tilde{u}_e|^4, \quad n_4 < 0 \tag{2.39}$$

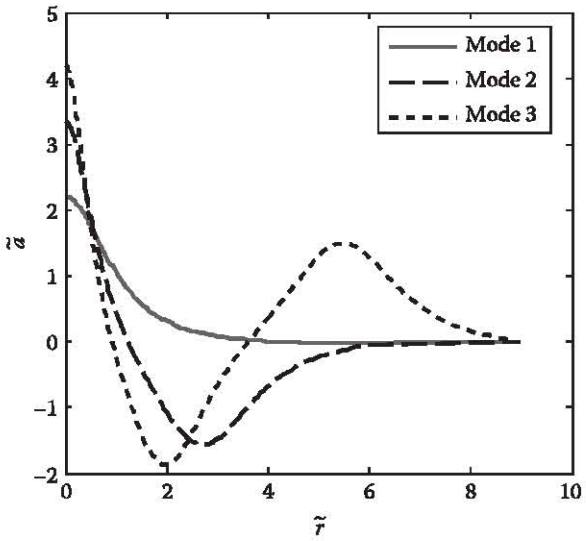

FIGURE 2.10 Townes soliton profiles for the first three "modes."

Incidentally, for the paraxial case, two transverse dimensions and assuming radial symmetry, and $\sigma = 1$, a special solution of (2.38), called the Townes soliton [7], can be found as the solution of the normalized differential equation

$$\nabla_{\perp}^2 R(r) - R + R^3 = 0, \quad R'(0) = 0, \quad R(\infty) = 0 \tag{2.40}$$

Typical solutions for three different initial conditions, called *modes*, are plotted in Figure 2.10. These modes, named $\tilde{a}(\tilde{r})$, are characterized by the fact that the solutions tend to zero for $\tilde{r} \to \infty$. The solutions of Equation 2.40 are very sensitive to initial conditions: for other initial conditions, the solutions do not converge to zero as $r \to \infty$.

The basic concept behind adaptive numerical algorithms is rather simple: imagine that a Gaussian beam is spreading during linear propagation due to diffraction. If a numerical solution is being computed, it is clear that after some distance of propagation, the size of the beam will become comparable to the total transverse grid size, which will result in errors in the numerical computation, such as aliasing if fast Fourier transform (FFT) techniques are used. The problem can be alleviated if the transverse profile is re-sampled using a coarser grid size. The step size for propagation can also be increased, based on the presumption that no sudden changes in the beam would occur at distances larger than the Rayleigh range. The converse should be true for beams that are focusing: the transverse grid size should be made finer and the propagational step size smaller.

In the case of the NLS equation, for the case $D = 2$, and assuming radial symmetry, McLaughlin et al. [14] predicted similarity solutions of the form

$$\tilde{u}_e(r,z) \propto \frac{1}{(z_r - z)^{1/2}} F\left(\frac{r}{(z_r - z)^{1/2}}\right) \tag{2.41}$$

where F is an arbitrary function. We can use this knowledge to adaptively vary the longitudinal stepping Δz and the transverse grid size for the beam.

A few more technical details must be mentioned before commencing the discussion on our adaptive numerical techniques. Weinstein [15] has shown that if the initial beam power P_0 is less than the lower bound for the critical power for blowup $P_c^{lb} = (\lambda^2/4\pi n_0 n_2)N_c$, where $N_c = \int |R|^2 r\,dr = 1.86225$, there

is no collapse of the paraxial NLS equation. Also, for an arbitrary initial profile $\tilde{u}_{e0} \neq R$, Fibich [13] proved that there is an upper bound for the critical power $P_c^{ub} = (\lambda^2/4\pi n_0 n_2)\, G(\tilde{u}_{e0})$ where

$$G(\tilde{u}_{e0}) = \frac{\left(2\int |\tilde{u}_{e0}|^2\, dr \int |\nabla \tilde{u}_{e0}|^2\, dr\right)}{\left(\int |\tilde{u}_{e0}|^4\, dr\right)}$$

for which blowup will occur for this initial profile if it has sufficient high power. There are few known integral invariants for the paraxial NLS equation above when $\sigma D \geq 2$. These invariants are based on the symmetry of the NLS equation under gauge, space, and time transformations, and may be derived from a Lagrangian density of Equation 2.37. Three of these invariants are the Hamiltonian and the variance, defined as [14,16]

$$N = \int |\tilde{u}_e|^2\, dr \tag{2.42a}$$

$$H = \int \left(|\nabla \tilde{u}_e|^2 - \frac{1}{2} |\tilde{u}_e|^4 \right) dr \tag{2.42b}$$

$$\frac{1}{8} \frac{d^2}{dz^2} \int |r|^2 |\tilde{u}_e|^2\, dr = H - \frac{D-2}{4} \int |\tilde{u}_e|^4 dr \tag{2.42c}$$

where the term $|\nabla \tilde{u}_e|^2$ results from diffraction, and $|\tilde{u}_e|^4$ from the nonlinear effect.

Note that from Equation 2.42c blowup occurs only if $D \geq 2$. The "variance" is given as $V(z) = \int |r|^2 |\tilde{u}_e|^2\, dr = 4Hz^2 + (dV(0)/dz)z + V(0)$ for $D = 2$ [17]. Thus, for $H < 0$, the function $V(z)$ vanishes at a distance $z_r = [V_0/-4H_0]^{1/2} > 0$. A sufficient condition for blowup is $H < 0$, i.e., when the nonlinear effect is stronger than diffraction, the beam self-focuses and collapse occurs at a distance $z_c \leq z_r$.

For an input Gaussian of the form $\tilde{u}_{e0} = ce^{-r^2/2r_0^2}$, $z_r = \left(1/(pN_c/2-1)\right)^{1/2}$, $z_c = 0.317(p-1)^{-0.6346}$ for $r_0 = 1$, and $z_c = 0.1585(p-1)^{-0.6346}$ for $r_0 = 1/\sqrt{2}$, where $p = N_0/N_c$ and $N_0 = c^2 r_0^D$ [18]. Note that the condition $H = 0$, which leads to P_c^{ub}, leads to an overestimate of the actual critical power.

We now outline our numerical adaptive spectral technique called the *adaptive split-step fast Hankel transform* (AFHTSS) used to track the solution of the NLS equation for $\sigma = 1$, $D = 2$ and variable ε. Our scheme is based on the combination of the standard split-step fast Fourier transform (SSFFT) and the Hankel transform, which exploits the cylindrical symmetry of the problem. This enhances the computation time and precision appreciably. In addition, we also use the concepts from the similarity solution developed by McLaughlin et al. [14] and apply them to our split-step spectral method mentioned above, so that the grid transverse spatial range and the longitudinal spatial step are adaptively updated. As its name indicates, we use the Hankel transform (see Chapter 1) instead of the usual Fourier transform, relying on algorithms already developed in the literature [19]. In cylindrical coordinates, Equation 2.38 becomes

$$\frac{\partial \tilde{u}_e}{\partial z} - j\varepsilon \frac{\partial^2 \tilde{u}_e}{\partial z^2} = j\left(\frac{\partial^2}{\partial r^2} + \frac{1}{r}\frac{\partial}{\partial r} \right) \tilde{u}_e + j|\tilde{u}_e|^2 \tilde{u}_e; \quad \tilde{u}_e(r, z=0) = \tilde{u}_{e0}(r) = c\exp -ar^2 \tag{2.43}$$

We use the definition of the lth order Hankel Transform pair [19,20]:

$$\Psi(\rho,z) = 2\pi\int_0^\infty \psi(r,z)J_l(2\pi r\rho)rdr, \quad \psi(r,z) = 2\pi\int_0^\infty \Psi(\rho,z)J_l(2\pi r\rho)\rho d\rho \tag{2.44a}$$

and the property:

$$j\left(\frac{\partial^2}{\partial r^2}+\frac{1}{r}\frac{\partial}{\partial r}\right)\psi(r,z) \xrightarrow{\text{HT}} -j4\pi^2\rho^2\Psi(\rho,z) \tag{2.44b}$$

The AFHTSS algorithm in Figure 2.11 resembles the symmetrized Fourier split-step technique, where we change the longitudinal spatial step $\Delta z \propto (1/c(z_1)^2 - 1/c(z_2)^2) \approx 1/c(z_1)^2$ when $c(z_2) \gg c(z_1)$, adaptively using McLaughlin's similarity formula (2.41) and the grid spatial range $\Delta r_{\max} \propto 1/c(z)$ in order to track the varying amplitude of the focusing beam when $\varepsilon = 0$.

There are several numerical approaches for implementing the Hankel transform [19,21]. The importance of Siegman's method [19] resides in the fact that, depending on the parameters, one can employ a non-uniform sampling that is denser near the focusing region, which has advantages over uniform sampling. Yu et al.'s method [21] is based on the expansion of the function and its transform by a zero order Bessel series that can be written as

$$\hat{\Psi}(m) = \sum_{n=1}^{N} C_{mn}\hat{\psi}(n), \quad \hat{\psi}(n) = \sum_{m=1}^{N} C_{nm}\hat{\Psi}(m) \tag{2.45a}$$

$$C_{mn} = \frac{2}{S}J_0\left(\frac{j_n j_m}{S}\right)\left|J_1^{-1}(j_n)\right|\left|J_1^{-1}(j_m)\right| \tag{2.45b}$$

$$\hat{\psi}(n) = \psi\left(\frac{j_n}{2\pi R_2}\right)\left|J_1^{-1}(j_n)\right|R_1, \quad \hat{\Psi}(n) = \Psi\left(\frac{j_n}{2\pi R_1}\right)\left|J_1^{-1}(j_n)\right|R_2 \tag{2.45c}$$

The j_n's are the positive roots of the zero order Bessel function J_0, J_1 is the first order Bessel function, and R_1, R_2 are the spatial and transform ranges respectively, with $S = 2R_1R_2$. For $r_n \in r \geq R_1$ and $\rho_m \in \rho \geq R_2$, we have $\psi(r_n) = \Psi(\rho_m) = 0$, where $r_n = j_n/2\pi R_2$ and $\rho_m = j_m/2\pi R_1$.

We now show sample simulation results using the AFHTSS method that uses Yu et al.'s Hankel transform technique [21], as well as a novel adaptive version of a split-step fast fourier transform (AFFTSS) technique. For the test function $\psi_0 = 4e^{-r^2/2}$, self-focusing and collapse is expected at $z_c = 0.1487$ for $\varepsilon = 0$. Note that $z_r = 0.288$, based on the study above, which is obviously overestimated. Figure 2.12 shows the maximal focusing as a function of grid size $h = \Delta r$, which proves the convergence of our method to the numerical focusing point when Δr decreases by varying the S parameter defined above [22]. Although the trend is similar, this is a considerable improvement over the convergence test results in Fibich and Ilan [23]. Figure 2.13 shows the growth of the on-axis intensity using AFHTSS technique for the test function above [22]. Also, in this figure, we take $S = 2\pi R_1R_2 = 2\pi \times 2000$ (corresponding to approximately 4000 cylindrical samples), which permits computation for the paraxial case till $z = z_c = 0.14817$ corresponding to the expected $z_c = 0.1487$ written above. Figure 2.14 shows the corresponding AFFTSS technique for 1024 x 1024 grid where we get $z = z_c = 0.1581$ [22]. This implies that the critical distance z_c is a little bit over estimated and the maximum intensity reached is also less than the AFHTSS method. It is instructive to note that with increase in sampling points, the AFFTSS approaches the results from AFHTSS, but on the

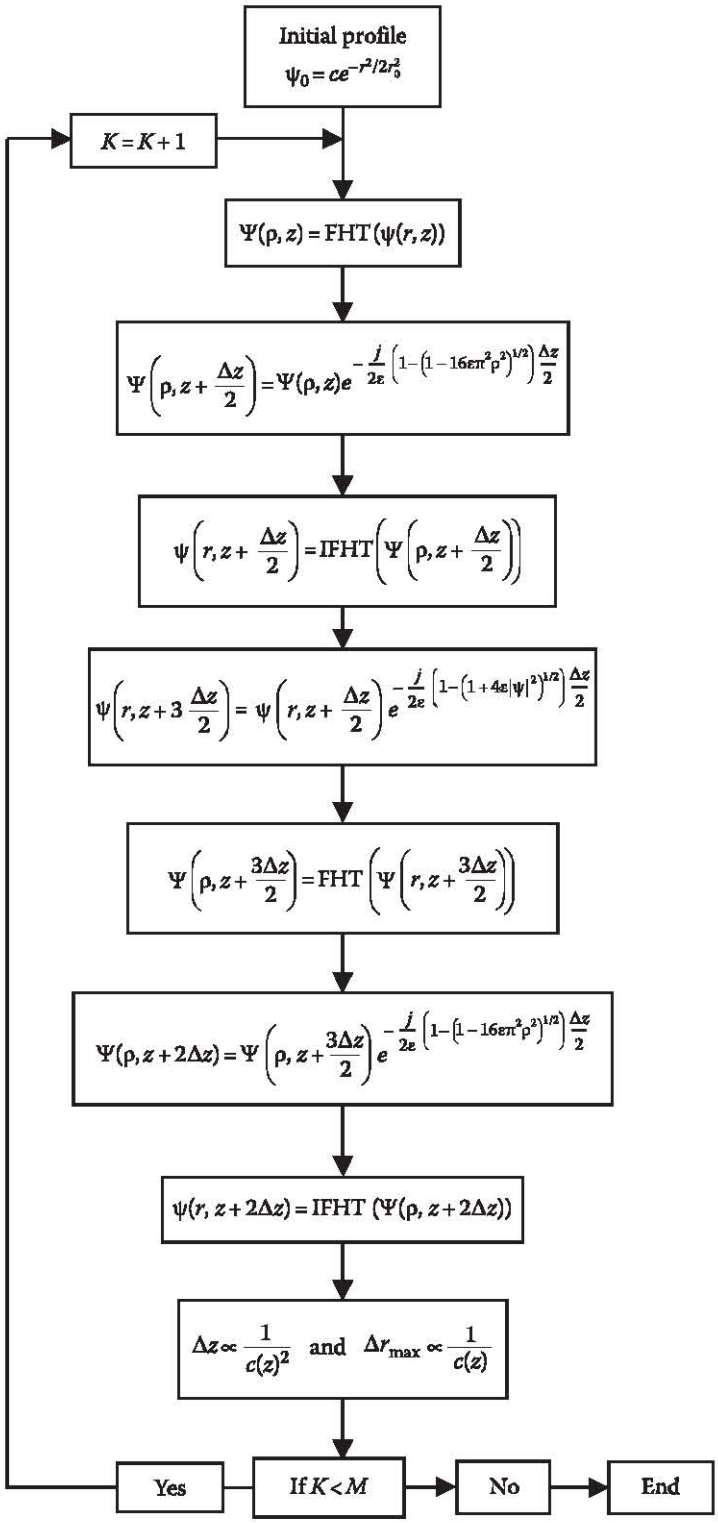

FIGURE 2.11 The AFHTSS algorithm, a symmetrized version of the split-step FFT using Hankel transform instead, and using adaptive longitudinal stepping and transverse grid management. FHT: fast Hankel transform, IFHT: inverse fast Hankel transform.

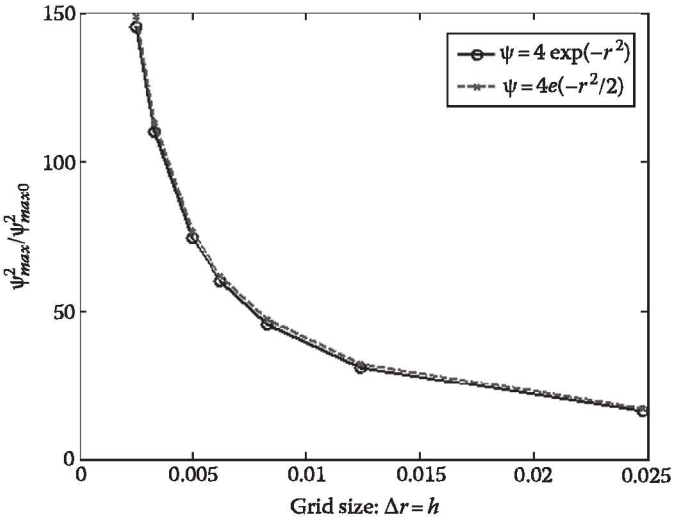

FIGURE 2.12 Maximal focusing as a function of grid size. (From Banerjee, P.P. et al., *Opt. Commun.*, 249, 293, 2005. With permission.)

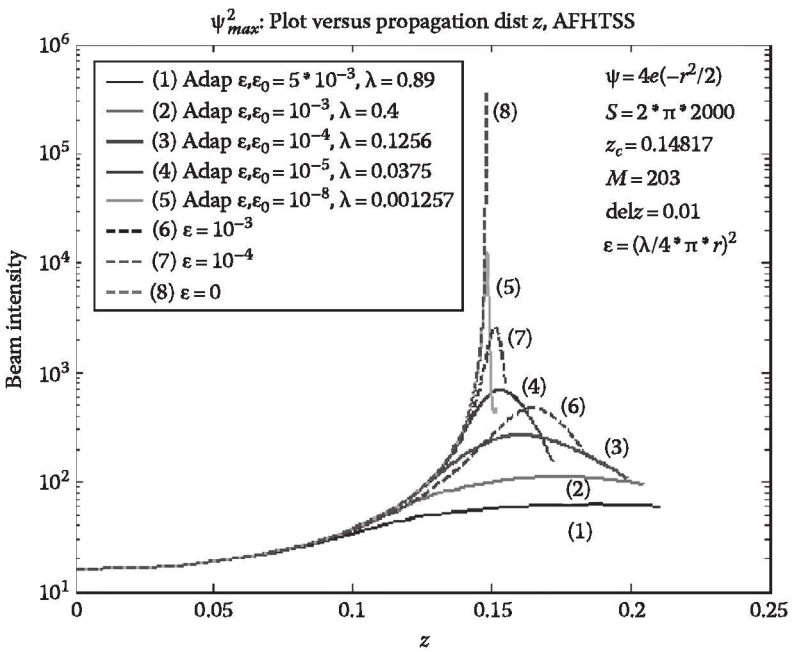

FIGURE 2.13 On-axis intensity of $\psi_0 = 4e^{-r^2/2}$ as a function of propagation for fixed values of ε ranging from 10^{-2} to 10^{-8} where $z = z_c = 0.1481$ for $\varepsilon = 10^{-8}$, and for an adaptive ε varying as $\varepsilon = (\lambda/4\pi r)^2$, using AFHTSS with $S = 2\pi R_1 R_2 = 2\pi \times 2000$ (4000 cylindrical samples). (From Banerjee, P.P. et al., *Opt. Commun.*, 249, 293, 2005. With permission.)

expense of calculation time. Also we note that changing the number of samples in both techniques does not affect the value of the critical distance drastically, but the maximum intensity reached at that point will be less or more depending on the number of samples, which is in agreement with the convergence test mentioned above. We stress that in all computations using AFHTSS and AFFTSS, energy is always conserved. Consequently, AFHTSS permits us to track peak intensities higher, faster, and more accurate than what is achievable by AFFTSS. Also, by using adaptive

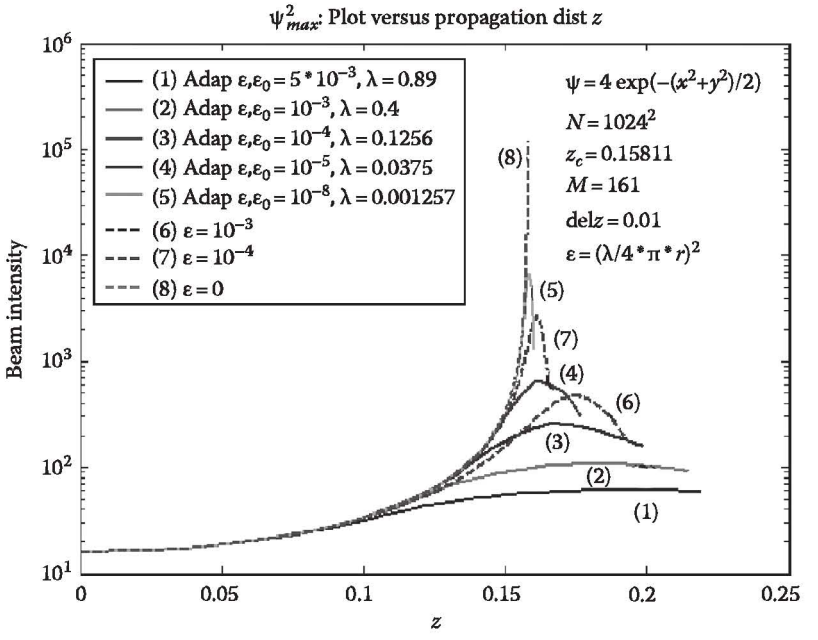

FIGURE 2.14 On-axis intensity of $\psi_0 = 4e^{-r^2/2}$ as a function of propagation for fixed values of ε ranging from 10^{-2} to 10^{-8} where $z = z_c = 0.1581$ for $\varepsilon = 10^{-8}$, and for an adaptive ε varying as $\varepsilon = (\lambda/4\pi r)^2$, using AFFTSS with 1024^2 samples. (From Banerjee, P.P. et al., *Opt. Commun.*, 249, 293, 2005. With permission.)

non-paraxiality parameter ε in the scalar nonparaxial equation, we obtain results similar to those of the more complex vector method [24] and superior to those when ε is constant [13].

Finally, we compare computation speeds of the AFHTSS and AFFTSS. It can be shown that for Siegman's method, the number of computations is proportional to $4N\log_2 2N + 2N$, compared with $2N^2\log_2 N$ computations for the two dimensional FFT as in AFFTSS. Although at first glance, the number of computations in Yu et al.'s method is proportional to N^2, we can make the number of computations comparable to Siegman's method by a priori computing and storing the zeros of the Bessel function. The advantages of Yu et al.'s method over Siegman's are the accuracy for the sampled points and a simple retrieval expression. For more comparison between Yu et al.'s and Siegman's method, we refer readers to table 1 in Yu et al. [21]. Also, we note that the use of the adaptive variation of the longitudinal propagation stepping size Δz and the transverse spatial sampling size according to $1/c^2(z)$ and $1/c(z)$ allow us to track on-axis amplitudes, for the paraxial case, up to two orders of magnitude more than what is achievable without the adaptive algorithm, for both the AFHTSS and AFFTSS methods. Without the adaptive variation, the numerical methods become unstable, and we witness oscillatory focusing and defocusing of the beam from numerical instability. Typical run times on a Pentium IV 2.4 GHz processor with a 2 GB RAM are around 1 min for AFHTSS when $S = 2\pi R_1 R_2 = 2\pi \times 2000$, 10 min for AFFTSS when the mesh size is $N^2 = (2^{10})^2$. Note that the Hankel transform based method, which exploits the cylindrical symmetry, is one dimensional, and therefore is expected to be faster than other two dimensional FFT based numerical methods.

2.7 BEAM PROPAGATION AND COUPLING IN PHOTOREFRACTIVE MEDIA

2.7.1 Basic Photorefractive Physics

In this section, a model for beam propagation through a nonlinear PR material that takes into account inhomogeneous induced refractive index changes due to the nonlinearity is first developed. In some cases a focused Gaussian beam asymmetrically distorts due to passage through the nonlinear material.

The PR effect has been used in a wide variety of applications, viz., image processing, optical interconnections, optical data storage, optical limiters, and self-pumped phase conjugators [25]. When a PR material is illuminated by a light beam or by a fringe pattern generated by the interference of two light beams, photoexcited carriers are redistributed in the volume of the crystal [25]. This sets up a space-charge field which, through the linear electro-optic effect, gives rise to a refractive index profile and hence a phase hologram.

The phenomenon of PR beam fanning, where the incident light beam is deflected and/or distorted when it passes through a high-gain PR crystal, has been observed in $BaTiO_3$, $LiNbO_3$, and SBN [26–28]. One of the ways this has been explained is through the fact that a symmetric beam may create an asymmetric refractive index profile, leading to beam distortion, or what we will call *deterministic beam fanning* (DBF) in the far field [29]. This analysis has been done for a thin sample, meaning one where diffraction of the beam is neglected during its travel through the PR material, and by using a linearized theory to determine the induced refractive index profile. We have recently extended the linearized approach to the case of a thick sample, and have included the transient effects, and are in the process of determining the effects of transient DBF when a reading beam is used to illuminate a previously stored hologram in the PR material [30].

Another school of thought is that beam "fanning" results from light scattering from the random distribution of space charges in the PR material. However, a larger contribution to *random beam fanning* (RBF) is the so-called amplified noise [31], which may arise from the couplings between the plane-wave components scattered from crystal defects.

In what follows, we examine steady state DBF in a diffusion-dominated PR material by deriving a closed form expression for the induced refractive index change from the nonlinearly coupled Kukhtarev equations. We also assess the role of propagational diffraction in DBF by determining the similarities and differences between the thin and thick sample models.

It must be stated that the simplified model for the induced refractive index described in the following sub-section can be also used to analyze two beam coupling and energy exchange in PR materials. When two approximately co-propagating beams are incident on the PR material, they give rise to *induced transmission gratings* which facilitate the energy exchange. On the other hand when two approximately contra-propagating beams are incident on the PR material, they give rise to *induced reflection gratings* which also facilitate the energy exchange. This energy exchange occurs over and above the beam fanning described above. While the first model described below for induced refractive index is based on carrier diffusion, other effects such as the *photovoltaic* (PV) effect in materials such as $LiNbO_3$ can also contribute to induced transmission and reflection gratings, as will be seen later.

2.7.2 Induced Transmission Gratings

It can be shown that the coupled set of simplified Kukhtarev equations [25] (see Chapter 6 for details) for a diffusion-dominated PR material can be decoupled in the steady state to yield an ODE for the space charge electric field [29]. In denormalized form, we can express this electric field $\vec{E}_s(x, y, z)$ approximately as

$$E_s \sim \frac{k_B T}{e} \frac{\vec{\nabla} I}{\beta / s + I} \tag{2.46}$$

where

e is the electronic charge
k_B is the Boltzmann constant
T is the temperature
s is the ionization cross section per unit photon energy
β is the thermal generation rate
$I(x, y, z)$ denotes the intensity distribution along x, y at a position z in the PR material

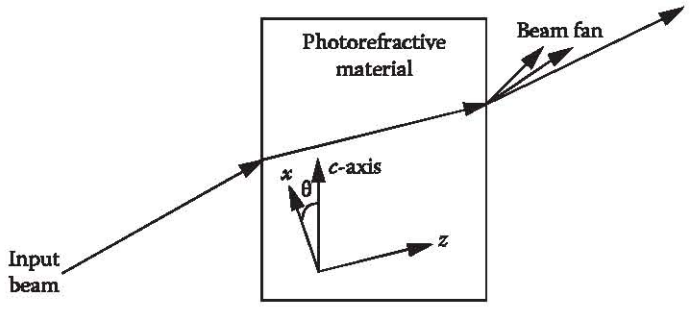

FIGURE 2.15 Geometry for analysis of DBF.

Now, this electrostatic field induces a refractive index change $\Delta n_{ext}(x,y,z)$ for extraordinary polarized (say along x, see Figure 2.15) *plane waves* of light in the PR material, assuming that $BaTiO_3$ in this example, through the linear electro-optic effect, is given by

$$\Delta n(x,y,z,\theta) = E_{sx}(x,y,z) f(\theta)$$

$$f(\theta) = -\frac{1}{2} n_e^3(\theta)\cos\theta(r_{13}\sin\theta + r_{33}\cos^2\theta + 2r_{42}\sin^2\theta) \tag{2.47}$$

$$n_e^2(\theta) = \left(\sin^2\frac{\theta}{n_0^2} + \cos^2\frac{\theta}{n_e^2}\right)^{-1}$$

where n_0, n_e are the linear ordinary and extraordinary refractive indices, and r_{ij} is the linear contracted electro-optic coefficient [25].

The angle θ in Equation 2.47 is defined in Figure 2.15. Note that $f(\theta)$ is a slowly varying function of θ over the spectral content of the optical field. It can be readily shown that, in general, propagation through the PR material under the slowly varying envelope approximation may be modeled by means of the PDE [29]

$$\frac{\partial E_e}{\partial z} = -jk_0\Delta n E_e - j\left[\frac{1}{2n_e(\theta)k_0}\right]\nabla_\perp^2 E_e$$

$$\Delta n(x,\theta) = \Im_x^{-1}\left[\Im_x[E_{sx}(x)] f\left(\frac{k_x}{n_e(\theta)k_0} + \theta\right)\right]$$

$$E_{sx}(x) = \frac{k_B T}{e}\frac{\partial |E_e(x)|^2/\partial x}{\eta\beta/s + |E_e(x)|^2} \tag{2.48}$$

For values of θ around 40°, a symmetric beam could induce an asymmetric refractive index profile, leading to beam bending and DBF in the far field. However, for some other value of θ, for instance 90°, our theory predicts symmetric beam shaping, in agreement with the findings of Segev et al. [31]. In this respect, the nature of the optical nonlinearity in a PR material is more involved as compared to that in a nonlinear Kerr-type material. We point out that in a Kerr-type material for instance, only an asymmetric beam profile can cause beam bending, as reported in [32], while a symmetric beam undergoes self-focusing or defocusing.

In what follows, we first provide results for the far-field beam profiles by assuming the PR material to be a thin sample, in the sense that we neglect the effects of propagational diffraction through the material. A Gaussian input

$$E_e(x,y,0) = (I_0\eta)^{1/2} \exp\left[-\frac{(x^2+y^2)}{W^2}\right] \tag{2.49}$$

with $I_0 = 2P/\pi W^2$, where I_0 denotes the on-axis intensity and P is the beam power, is phase modulated due to the induced refractive index profile. The resulting output field is $E_e(x,y,L) = E_e(x,y,0)$ $\exp(-jk_0\Delta n(x)L)$, where L is the thickness of the PR material. Such a phase modulation results in a shift of the far-field pattern with respect to the axis (z) of propagation of the optical beam, and in the appearance of asymmetric sidelobes, the so-called fanning of the beam. Numerical simulations for $BaTiO_3$ with parameters $n_0 = 2.488$, $n_e = 2.434$, $r_{42} = 1640$ pm/V, $r_{13} = 8$ pm/V, $r_{33} = 28$ pm/V, $s = 2.6 \times 10^{-5}$ m^2/J, $\beta = 2$/s, $T = 298$ K [29] and $L = 1$ cm and using an incident wavelength of 514.5 nm shows a monotonic increase in the shift of the far-field main lobe from the z axis with increase in I_0 (implying either an increase in power P or a decrease in width W). In Figure 2.16a and b, k_x is the spatial frequency variable corresponding to x, and is related to the far-field coordinate x_f by $k_x = k_0 x_f/d$, d being the distance of propagation from the exit of the crystal to the far field [29]. However, the amount of DBF (defined by the relative amount of power in the sidelobes) varies nonmonotonically with intensity, initially increasing as the intensity is increased from low levels to attain a maximum, and then decreasing with further increase in intensity.

Note that our results are different from those of Feinberg [26], in that the latter, based on a linearized *two-beam coupling* (TBC) theory that neglects coupling of the angular plane wave components of the Gaussian with any background illumination, yields $\vec{E}_s \propto \vec{\nabla} I/I_0$, where I_0 is the quiescent intensity (to be compared with our Equation 2.48). For a Gaussian intensity profile, the locations of the extrema of E in Feinberg's formulation are fixed w.r.t. to the incident profile, and hence may be shown to predict a monotonic increase in DBF with a decrease in W. In our nonlinear formulation, however, for decreasing W, the extrema of E move out with respect to the incident profile, so that the profile essentially sees a linear induced refractive index for sufficiently small W resulting in reduced DBF.

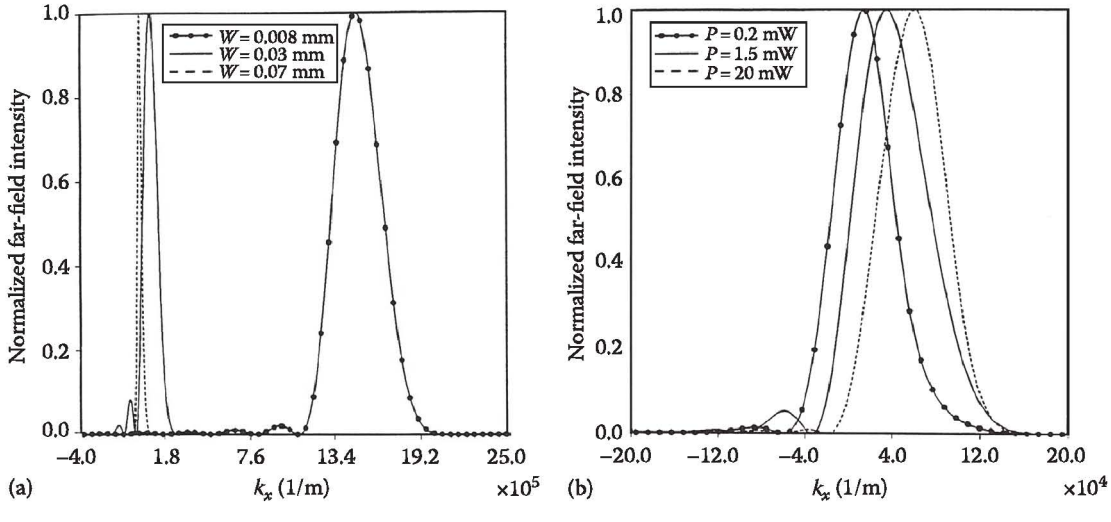

FIGURE 2.16 Normalized far-field intensity profiles for the thin-sample model: (a) P = 1.5 mW and (b) $W = 40\,\mu$m. (From Banerjee, P.P. and Misra, R.M., *Opt. Commun.*, 100, 166, 1993. With permission.)

Before comparing the thin sample results with the findings for the thick sample case, we will, at this point, provide a simple alternate explanation for the observed behavior of DBF when monitored as a function of the intensity. Our explanation is based on the examination of the spectrum of the phase modulation $\exp(-jk_0\Delta n(x)L)$. The far-field pattern is the convolution of the above spectrum with that of the input profile. Since $\Delta n(x)$ is an odd function of x (see Equations 2.47 and 2.48), it can be expanded in a power series of the form $ax^3 - bx$, where a and b are given by

$$b = \frac{4f(\theta)k_BT/eW^2}{\beta/sI_0 + 1}, \quad a = \frac{(2b/W^2)(\beta/sI_0)}{\beta/sI_0 + 1} \tag{2.50}$$

Note that the coefficients of this expansion hold for all values of the ratio β/sI_0. The spectrum $H(k_x)$ of $\exp(-ik_0\Delta n(x)L)$ is then

$$H(k_x) = \frac{2\pi}{(3a)^{1/3}} Ai\frac{k_x - bk_0L}{(3a)^{1/3}} \tag{2.51}$$

Once again, k_x has the same implication as in the discussion on Figure 2.16. We comment that if d is replaced by f, where f is the focal length of a lens at the exit plane of the crystal, k_x, and hence x_f, would be representative of the spatial coordinate on the back focal plane of the lens. Ai[.] is the *Airy function* [33]. The ith zero, α_i, of $H(k_x)$ is related to the ith zero, γ_i (<0) of Ai[.] by $\alpha_i = bk_0L + (3a)^{1/3}\gamma_i$. It then follows that the spatial extent of the Airy pattern for $k_x < bk_0L$, up to say the ith zero, and normalized by the spectral width $2/W$ of the incident Gaussian profile, varies nonmonotonically with I_0. The shift in the Airy pattern, bk_0L, however, increases with an increase in I_0. For large I_0, it can be shown that the shift is proportional to $1/W^2$, in agreement with the trend in Figure 2.16a. The resulting far-field pattern which is the convolution of the Gaussian spectrum and the Airy pattern generally exhibits decreased DBF when the Airy pattern has a (denormalized) width much smaller than that of the Gaussian spectrum (which may occur, for instance, for both small and large W). This is in agreement with our numerical simulations in Figure 2.16. Appreciable DBF occurs in the region where the normalized spectral width is greater than unity. As an example, for $P = 1.5$ mW, maximum beam fanning, defined by the maximum of the ratio of the peak value of the sidelobe and that of the mainlobe, occurs when $W = 30\,\mu$m. Details can be found in Misra and Banerjee [29].

We will now present the results for the far-field beam profiles using a thick sample model for the PR material and point out the similarities and differences with the thin sample approach. Numerical simulations for the thick sample model were performed on the basis of Equation 2.48 by employing the split-step beam propagation technique discussed above. In this simulation, we track both the phase and amplitude modulation of the beam within the crystal due to the combined effects of propagational diffraction (along x, y) and induced refractive index (along x) arising from the PR effect. Figure 2.17a and b shows the normalized far-field intensity patterns with W and P as parameters. By W, we now mean the beam waist which would be expected at $z = L/2$ (i.e., the location of the center of the sample) in the absence of any electro-optic effect ($r_{ij} = 0$) (see inset in Figure 2.17a). The results are qualitatively similar: DBF is seen to reduce at very low (high) and very high (low) values of P (W). Quantitatively, for a fixed power P (viz., 1.5 mW), we can predict the absence of DBF for sufficiently large values for W (viz., 70 μm), which are independent of the model (thin or thick sample) used for simulation. Physically, this makes sense since the thin and thick sample models must agree if the diffraction effects in the crystal are sufficiently small. On the other hand, the reason for the absence of DBF for a sufficiently small value of W in the thick sample approach is that effectively, the beam width, if monitored over most of the sample is large (due to a large diffraction angle), implying a reduced PR effect. This, in turn, implies that propagation through the crystal is predominantly diffraction limited. For small W, the thick sample model therefore is more accurate than the corresponding thin sample model for the same value of W since the latter model

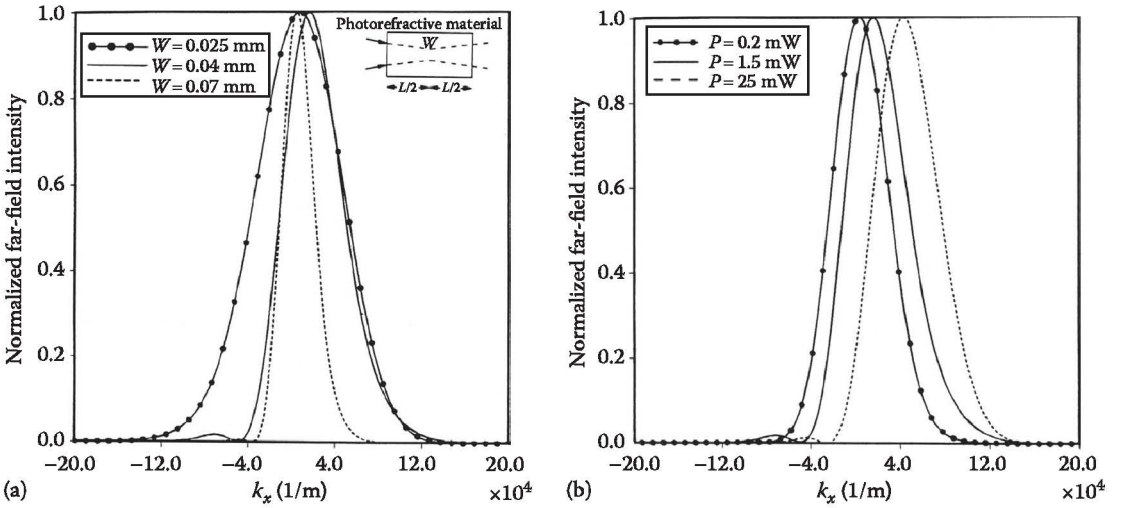

FIGURE 2.17 Normalized far-field profiles for the thick sample model: (a) $P = 1.5\,\text{mW}$ and (b) $W = 40\,\mu\text{m}$. (From Banerjee, P.P. and Misra, R.M., *Opt. Commun.*, 100, 166, 1993. With permission.)

overestimates the amount of cumulative PR effect. For the thick sample model, for the same value of P as above, we see negligible DBF for W less than $25\,\mu\text{m}$. On the other hand, the thin sample model predicts a value of W less than $5\,\mu\text{m}$ for negligible beam fanning. The reason for the disappearance of DBF in the thin sample approach has been presented above using the Airy function argument and the movement of the extrema of E w.r.t. the incident optical field. Maximum DBF for $P = 1.5\,\text{mW}$ occurs for $W = 40\,\mu\text{m}$, in close agreement with the thin sample computations and the Airy function approach. However, the shift in the position of the mainlobe in the thick sample model is much smaller as compared to the thin sample case due to the effective decrease in the PR effect for a small waist size, as explained above. Referring to Figure 2.17a, we note that for $W = 40\,\mu\text{m}$, $P = 1.5\,\text{mW}$, and $f = 10\,\text{cm}$, the spatial shift in the back focal plane of a lens of focal length f located at the exit plane of the PR material is about 0.2 mm. We would like to comment that for the above parameters, DBF was also numerically observed at the exit face of the thick PR sample.

Thus far we have analyzed the propagation of a single focused Gaussian beam in a diffusion-dominated PR medium. When two beams are incident on such a medium with a small angle between each other, the induced refractive index profile is responsible for energy exchange between the two beams, a phenomenon referred to as TBC. This energy exchange occurs due to the phase shift between the intensity interference pattern and the induced refractive index pattern [25]. We can effectively study the interaction and the resulting energy exchange between two focused Gaussian beams incident on the material numerically using the split-step method. The problem geometry is shown in Figure 2.18. The two Gaussian beams are focused in the center of the PR material and the angle between them is 2θ. The Gaussian beams are expressed in terms of their q-parameters (see Section 2.4) at the entry face of the material. The split-step algorithm is used to determine the interaction and energy exchange between the two beams. The induced refractive index Δn is used to construct the operator representing the induced inhomogeneity in the material. The results on two

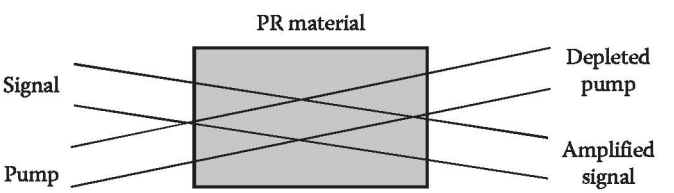

FIGURE 2.18 Geometry for TBC in a diffusion-dominated PR material.

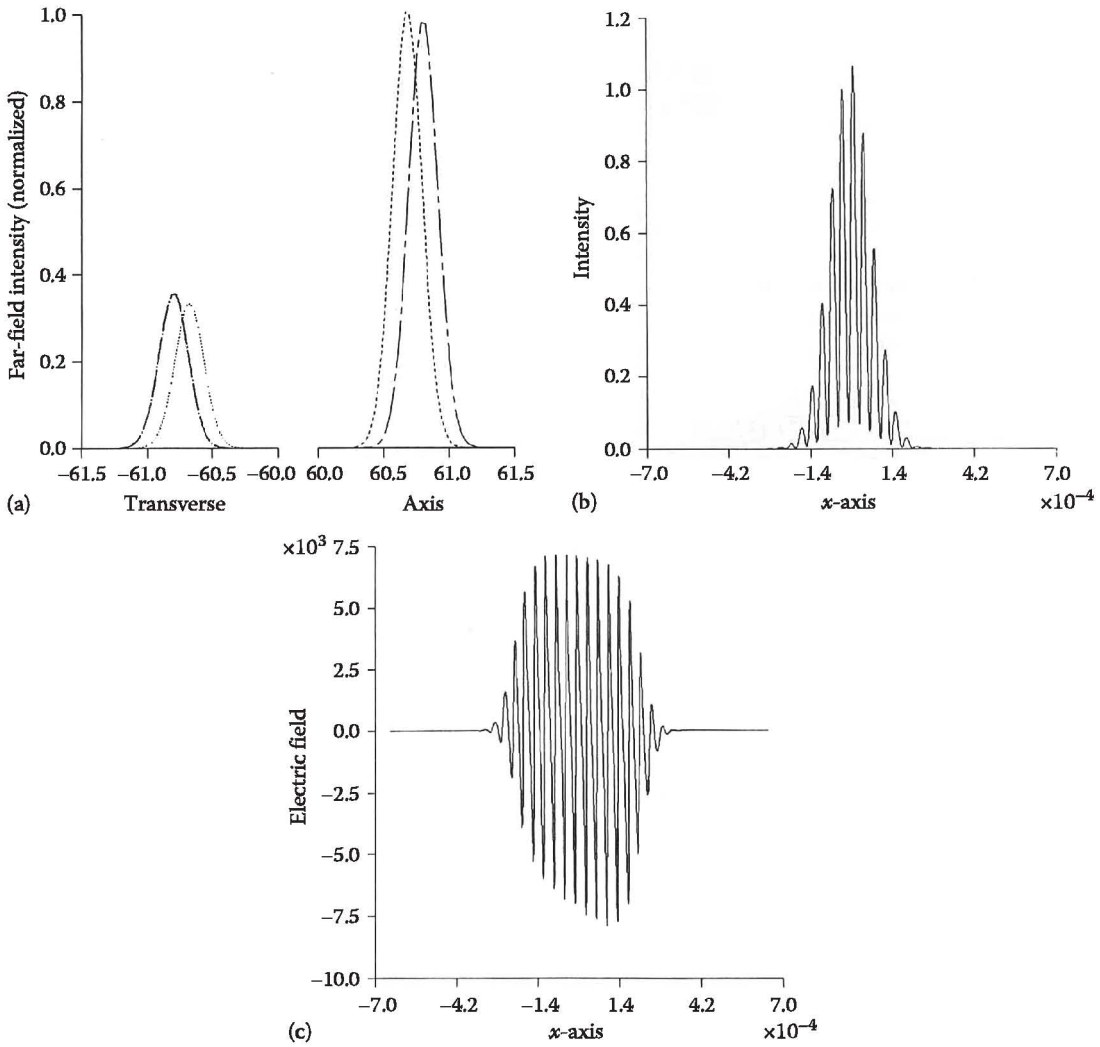

FIGURE 2.19 (a) Dotted and dashed lines are respectively the far-field signal and pump intensities with the absence of any PR material and chain dots and chain dashes represent the resulting far-field intensities after the beams have propagated through a 5 mm $BaTiO_3$ sample. Incident beams are focused to the center ($z = L/2$) of the PR crystal and the waist of each beam at wavelength 0.632 μm is 100 μm. Signal to pump ratio is 3 and semi-angle of crossing θ is 0.5°. (b) Interference pattern at center ($z = L/2$) of the PR crystal for the beams described in (a). (c) Space-charge field (V/m) at the center ($z = L/2$) of the crystal for the beams of (a). (From Ratnam, K. and Banerjee, P.P., *Opt. Commun.*, 107, 522, 1994. With permission.)

wave mixing are shown in Figure 2.19. The dot-dashed lines show the far-field intensity profiles of the two Gaussian beams in the absence of the PR material. The dashed lines show the beams after energy transfer due to the induced refractive index. The initial pump to signal power is 3. The peak intensity of the pump and signal beams are 63 and 21 W/cm^2, respectively, before the interaction. The beams are coupled by a 5 mm $BaTiO_3$ PR material. The output beams do not show any effect of beam fanning at this power; however, with larger beam powers, distortion of the beams due to beam fanning is observed. The results have been used to find the TBC strength and their dependence on the intensities of the two participating beams. The results, discussed in more detail in Ref. [34], depict that the coupling strength depends on the power ratio between the two beams, a fact that is ignored in perturbation calculations of two-wave mixing in PR materials. Later, in Chapter 6, we will analyze this effect in more detail with participating plane waves and using rigorous coupled wave theory.

2.7.3 Induced Reflection Gratings and Bidirectional Beam Propagation Method

Contrary to transmission gratings which are induced in a PR medium by two waves nominally traveling at a small angle with each other, reflection gratings are formed by two nearly contra-propagating waves. In a PR material such as lithium niobate ($LiNbO_3$), this can be simply formed due to the interference between an incident beam (typically traveling down the c-axis) and its Fresnel reflection from the back surface of the crystal due to the linear refractive index mismatch. The period of the reflection grating is therefore much smaller than that of the transmission grating, determined by the wavelength of the interacting waves (or beams). Energy exchange between the forward and backward traveling beams can give rise to depletion of the forward traveling beam (pump) and amplification of the backward traveling beam (signal), and has applications in optical limiting [35,36]. In what follows, we outline the use of the BPM, suitably modified to include forward and backward propagation, to determine the energy exchange during self-pumped TBC in a reflection grating geometry. It turns out that a PR material like $LiNbO_3$ has contributions to its PR effect from diffusion as well as the PV effect, where the latter gives rise to an induced refractive index profile in phase with the intensity profile, further complicating the analysis.

The bi-directionality of the simulation (opposing directions of the pump and signal beams) is handled by treating the two counter-propagating directions in sequence and then using an iterative shooting method to find the converged solution. The schematic of the beam propagation algorithm is shown in Figure 2.20. The dark lines on the left and right sides of Figure 2.20 represent the front and rear surfaces of the PR material, respectively, and the crystal c-axis is perpendicular to these faces. In this work, we only consider the case of $LiNbO_3$, which is a uniaxial crystal. For uniaxial crystals with light propagation along the polar axis, only one transverse polarization vector is required to be defined. The crystal longitudinal propagation direction is split into n steps (shown by the dashed lines). The incident pump beam is defined with a Gaussian amplitude profile and the e^{-1} spot size characterizes the focusing condition. Other transverse beam profiles may be substituted for the Gaussian, to suit specific experimental parameters.

In typical practical applications, the pump beam is usually chosen to be focused at the front surface of the crystal. Focus at any point inside the crystal is accomplished by doing beam propagation in a crystal through the desired length, taking the complex conjugate of the field and using that as the initial field. The amplitude of the incident optical field E_{in} is adjusted to use any desired power for the pump beam. During simulation, the field retains both amplitude and

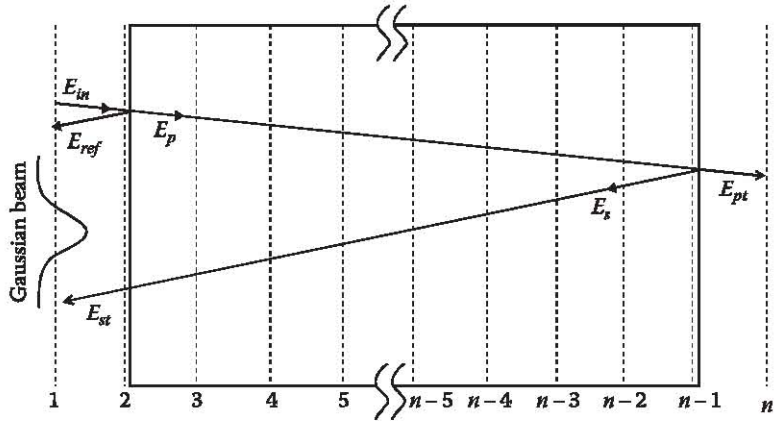

FIGURE 2.20 A schematic representation of the origin and path of the pump and signal beams. The signal beam (E_s) is generated by the Fresnel reflection of the pump beam (E_p) at the rear surface of the crystal. Both beams are nominally perpendicular to the boundaries. The paths are shown with angles to help distinguish the beams.

phase information at every propagation step. The paraxial approximation used in this split-step method allows us to simulate the propagation of beams with spot sizes as small as 3 μm without significant error [37].

As the beam enters the crystal (at step 2), part of it is reflected (E_{ref}). The transmitted beam (E_p) is propagated to the rear boundary, where part of this beam is transmitted (E_{pt}) and remainder is reflected (E_s) (at step $n-1$). At each propagation step, the local value of the pump field ($E_p(i)$) is saved in a buffer. The signal beam, E_s, is then propagated in the opposite direction to the pump beam, until it travels through the front face of the crystal (E_{st}). At each step the signal beam field $E_s(i)$ is also saved in a buffer. The $E_s(i)$ buffer is then added to the previously buffered pump beam field $E_p(i)$ to produce the interference array. At the ith longitudinal step, the intensity of the interference pattern is then given by $|E_p(i) + E_s(i)|^2$. Since the fields are defined as transverse arrays, the interference at every ith longitudinal step also has a transverse profile. This transverse profile of the interference, however, is computationally very costly, since for each step this has to be saved in the buffer. Moreover, since we are simulating an interference pattern, the step size along the longitudinal direction must be substantially smaller than the wavelength.

It is determined that for a crystal of thickness of the order of the wavelength (in the material), the number of points n has to be at least 40 to produce a smooth interference pattern. For contra-directional TBC in $LiNbO_3$, it is the intensity modulation in the longitudinal direction that is of greatest importance, since the electro-optic coefficient is weak perpendicular to the c-axis. Hence, we have employed an alternate approximate method of simulating the interference with less computational load. We have saved only the peak of the field (instead of the whole transverse array) in the buffer. This results in an interference pattern without a transverse profile. This approximation does not result in any significance difference in our simulation, but has improved the required CPU time by two orders of magnitude.

Figure 2.21 shows the peak of the interference at every step in the longitudinal direction (each point of the plot represent the peak of the transverse profile at that step) for a thin $LiNbO_3$ crystal. The length of the simulated crystal equals two wavelengths inside the crystal, where the free-space wavelength $\lambda_{\tilde{0}}$ is taken to be 532 nm, and the ordinary refractive index (n_0) of $LiNbO_3$ is used. Because there is no absorption loss and hardly any beam diffraction in this short distance, the interference has constant amplitude. For large crystal lengths, and for smaller beam spot sizes focused at the entrance of the crystal, the beam amplitude changes with propagation due to diffraction, and consequently results in a gradually decaying interference pattern.

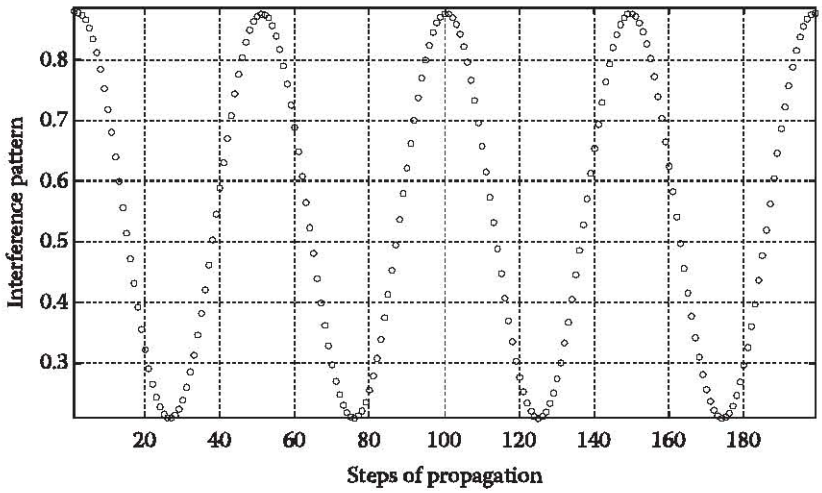

FIGURE 2.21 Interference pattern in the longitudinal direction for a $LiNbO_3$ crystal. Crystal length is equal to two wavelengths (532 nm) of light (inside). The number of longitudinal steps (n) per wavelength is 100. Spot size is 5 μm.

Following the linear cycle, the PR effect is now simulated through a nonlinear cycle of beam propagation. In this cycle, the buffered modulated intensity can be used to determine the space-charge field. The change in index then can then be determined by considering the electro-optic effect. For qualitative simulation, the following simplified general expressions are used [38,39]:

$$n = n_0 + \Delta n \tag{2.52}$$

$$\Delta n \propto E_s \tag{2.53}$$

$$E_s(\text{diffusion}) = C_{df} \cdot \nabla I(x, y, z) \tag{2.54}$$

$$E_s(\text{photovoltaic}) = C_{pv} \cdot I(x, y, z) \tag{2.55}$$

where n_0 is the bulk index of refraction of the crystal, and Δn is the change in index due to the space-charge field.

Note that in writing (2.54), we have approximated Equation 2.46 for the case where the "dark intensity" which may include background illumination is much larger than the intensity interference pattern from the participating optical waves or beams involved in coupling ($\beta/s \gg I$). Furthermore, in $LiNbO_3$, there is a substantial PV effect, which provides an additional contribution to the space charge field, as shown through Equation 2.55. The total space-charge field is approximately the sum of the contributions from diffusion of charge carriers and the PV effect.

The nonlinear cycle proceeds in a similar manner to the linear cycle. The buffered interference pattern intensity profile from the linear cycle is used to estimate the modified local refractive index variations through Equations 2.52 through 2.55. The refractive index change at each space-step in the calculations is treated as a dielectric boundary. As the pump beam E_p propagates through the index modulated crystal, the power of the beam is diminished at every step due to reflection losses at the dielectric boundaries, and the local values of E_p are stored in a buffer. Each grating reflected beam from the pump (pumpscatter) is propagated all the way out of the crystal. This grating scattered light is added to the buffered signal array. Each grating reflected beam from the signal (going toward the back surface of the crystal) is propagated all the way out of the crystal and added to the buffered pump array. As a first order approximation, it is assumed that scattered light from the pump and signal beams do not go through additional scattering during the propagation through the grating.

At the end of this first nonlinear cycle, the interference pattern is slightly modified. Subsequent iterations of this nonlinear cycle continue to modify the interference pattern (and the modulated index). When the difference between two successive interference patterns is within a chosen tolerance value (we have used 5%), convergence is assumed and the TBC efficiency is determined. All of the scattered beams that exit through the front and rear faces of the crystal are summed ($E_{p(scatter)}$ and $E_{s(scatter)}$ respectively). Throughout the crystal, the value of the pump buffer and signal buffer reflects the converged value of the pump and signal after loss or gain. In the case of pure charge diffusion, for the c-axis oriented along the direction of pump propagation, constructive interference occurs for the backscattered light, while the transmitted light suffers destructive interference. This interference occurs due to the phase difference between the interference and grating patterns, and the phase change in the scattered beams due to the reflections from the grating. The constructive and destructive interference directions are reversed when the crystal c-axis is reversed. Because of the destructive and constructive interference, the pump beam and the signal beam losses and gains power in the direction of respective propagation.

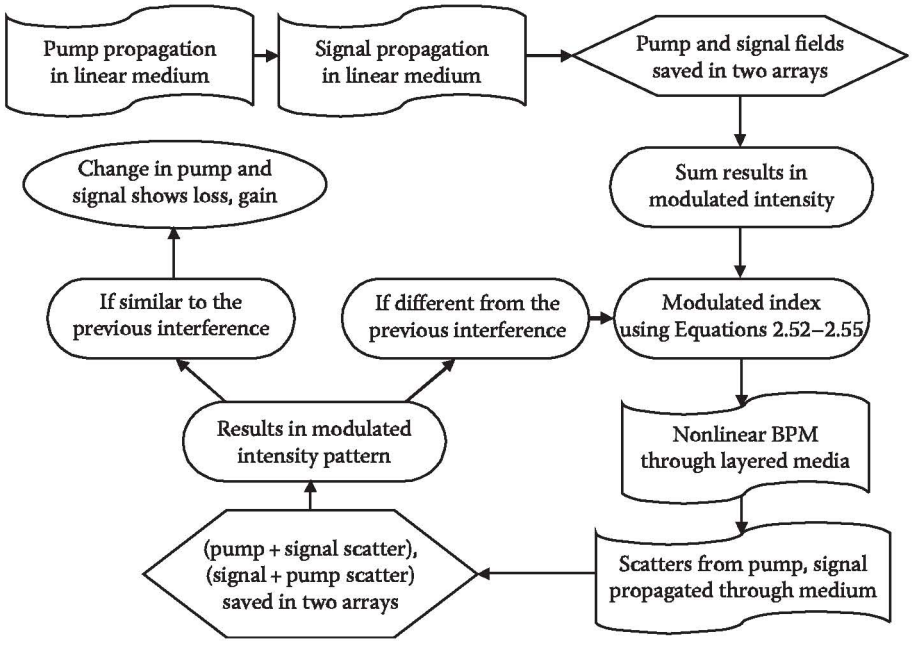

FIGURE 2.22 Flowchart showing the novel algorithm for simulation of self-pumped contra-directional TBC for a Gaussian beam.

This algorithm for self-pumped contra-directional TBC is summarized in the flowchart of Figure 2.22.

As stated earlier, a grating can only cause power coupling between two counter-propagating plane waves if the grating is phase shifted (ideally, by 90°) with respect to the interference produced by the two waves. For a grating that is in phase with the interference pattern, there can be no beam coupling. Extending on this established fact, we assume that for a weakly focusing beam, similar beam coupling behavior should be observed. We simulate a beam-coupling where the grating is 90° phase shifted with the interference (Figure 2.23), and in a crystal that is 2 wavelengths long. Following Equation 2.50, we have chosen C_{df} such that the change in index is 0.027. Figure 2.24 shows the

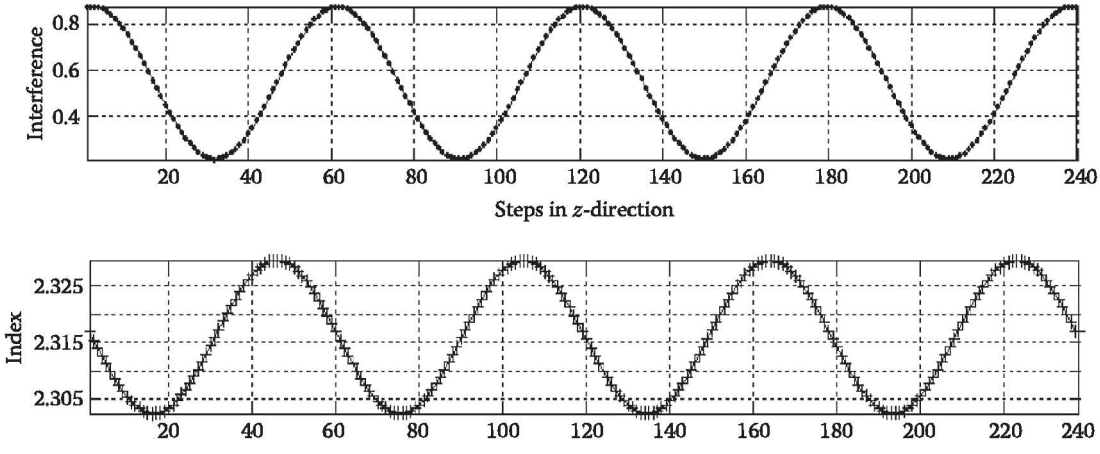

FIGURE 2.23 Interference pattern (top) and resulting 90° phase shifted index modulation (bottom) for pure diffusion alone. Crystal length is 2 wavelengths inside. Power inside is 1 unit and change in index is 0.027. (From Saleh, M.A., Self-pumped Gaussian beam coupling and stimulated backscatter due to reflection gratings in a photorefractive material, PhD dissertation, University of Dayton, Dayton, OH, 2007.)

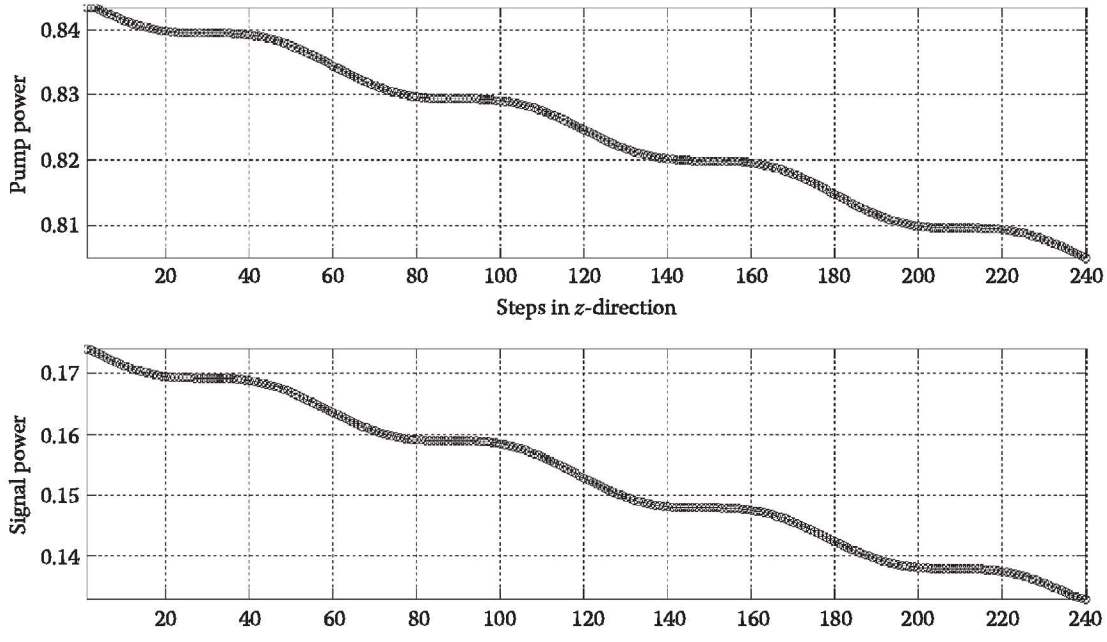

FIGURE 2.24 Energy exchange between the pump and the signal beam due to the modulated index from pure diffusion. Pump power is reduced by about 4% and signal power gains equally. Oscillation in power is artifact, as explained in the text. (From Saleh, M.A., Self-pumped Gaussian beam coupling and stimulated backscatter due to reflection gratings in a photorefractive material, PhD dissertation, University of Dayton, Dayton, OH, 2007.)

energy exchange between the pump and the signal beam due to the out-of-phase induced refractive index. Scattered light from the signal beam destructively interferes with the pump beam to diminish the pump power. Conversely, scattered light from the pump beam constructively interferes with the signal beam to increase the signal power. This is a distinctive feature of energy exchange due to beam coupling. In this case of simulation, pump power is reduced by about 4% and signal power gains equally. The observed oscillation in the power in Figure 2.24 is an artifact. The oscillation comes from the difficulty of calculating the power of (pump + signal scatters) or (signal + pump scatter) at any given point inside the nonlinear medium. The actual coupling is calculated by accounting for the amplified signal or diminished pumps outside the crystal, where the index is constant.

The presence of PV field usually has a negative effect on the phase of the index modulation. However, the PV field may change the magnitude of Δn to overcome this negative effect. It has been shown, both theoretically and experimentally, that a larger PV field may actually enhance the beam coupling [40]. This can also be verified using a constant value for C_{df} and changing the value of C_{pv} in our model Equations 2.52 through 2.55.

2.8 *z*-SCAN METHOD

The previous examples illustrated the use of the split-step method in calculating the beam profiles during diffraction in space or during propagation through a guided (externally or internally induced) medium. If a Gaussian beam is however assumed, the split-step method can be reformulated in terms of a differential equation that shows the evolution of the Gaussian beam's parameters, e.g., width, during propagation. The ensuing equation can be exactly solved in some cases, e.g., for a Kerr-type material, and is therefore physically more transparent than the results obtained using the split-step method. The differential equation for the parameter(s) may not be simpler to solve than the split step, however, having an analytical solution (Gaussian beam) adds a tremendous insight into the actual propagation of the wave through the material, whereas the split-step method

only presents simulation results. Using Equations 2.23a and 2.23b, when a Gaussian beam travels a distance Δz in an n_2 medium, the q-parameter change using the split-step method can be written as

$$\Delta q = \Delta z + \frac{q^2}{f_{ind}(\Delta z)} \tag{2.56}$$

where f_{ind} is the nonlinearly induced focal length of the slice Δz [7,41]. The above equation shows that the q of a Gaussian beam changes due to propagational diffraction and due to the induced nonlinearity of the material. In $LiNbO_3$, the PV effect is mainly responsible for breaking the circular symmetry of an incident focused extraordinarily polarized Gaussian beam. Therefore, the propagation model is based on the propagation of an elliptical Gaussian beam.

Light induced scattering resulting in DBF has been observed in PR $LiNbO_3$, and can be explained on the basis of an induced nonlinear refractive index primarily due to the PV and thermal effects [38]. This type of beam fanning is distinct from RBF due to light scattering from the randomly distributed space charges or crystal defects [31]. In $LiNbO_3$ the PV effect is responsible for breaking the circular symmetry of an incident focused extraordinarily polarized Gaussian beam in the far field, while the thermal effect manifests itself in circularly symmetric far-field patterns [38]. Over a range of input powers the PV effect dominates, resulting in an elongated far-field pattern with the spreading dominant along the c-axis of the crystal.

An interesting consequence of monitoring the q-parameter variation of a Gaussian beam as it propagates through a nonlinear material is the fact one can thereby estimate the amount of nonlinearity in the material. Conventional methods of estimating the sign and magnitude of the optical nonlinearity in materials include the z-scan technique where the far-field on-axis transmittance is monitored as a function of the scan distance about the back focal plane of an external lens [41–43], as shown in Figure 2.25.

We point out that sometimes the z-scan method, however, may be rather cumbersome since it involves physically scanning the material, leading to our development of a simpler technique where the longitudinal position of the sample is not changed. Instead the beam ellipticity is monitored as a function of the incident beam power P, while testing materials with induced inhomogeneous nonlinearities, e.g., PR $LiNbO_3$ [44]. Another disadvantage of the z-scan is that monitoring the on-axis intensity may be difficult due to aberrations, optical misalignments, sample imperfections, refractive index mismatch, and non-parallelism of the entry and exit faces of the material. The imperfections can give rise to fine interference patterns within the far-field intensity profile. These problems have been observed during z-scan measurements of $LiNbO_3$, leading us to develop the P-scan technique as an attractive and simple alternative [44].

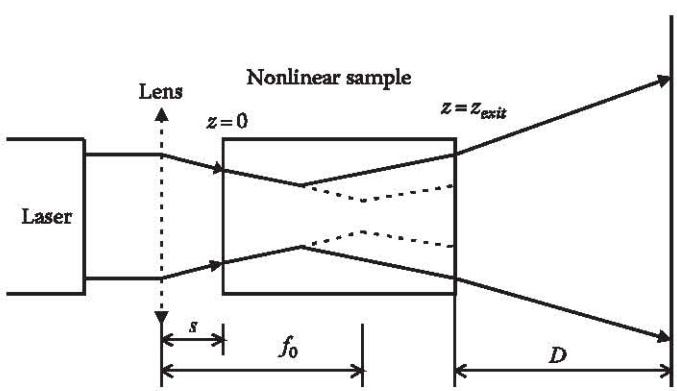

FIGURE 2.25 z-scan setup for a thick sample. The thick lines represent the path of the "rays," described as the locus of the $1/e$ points of the Gaussian beam. The thin lines show the ray path in the absence of the medium. Circular symmetry of the Gaussian beam is assumed throughout the sample.

In what follows, we develop the theoretical model for determining the nonlinear refractive index of PR $LiNbO_3$ that uses an appropriate model for beam propagation through a nonlinear material. The model takes into account inhomogeneous induced refractive index changes due to the optical nonlinearity. For the case of $LiNbO_3$, induced refractive index changes are primarily due to PV contributions over the range of powers used. The model is based on the evolution of beam widths of an incident circularly symmetric Gaussian beam focused by a lens onto the material in order to reduce RBF. The calculations closely follow the analysis for the z-scan determination of nonlinearities in a *thick* sample of a nonlinear material [41,44]. Under certain approximations, the model reduces to that used by Song et al. to study anisotropic light-induced scattering and "position dispersion" in PR materials [43]. Since we consider a "thick" sample, i.e., a sample whose thickness is much larger than the Rayleigh range of the focused Gaussian beam, diffraction effects become important and cannot be neglected. Therefore we determine the beam shape as it leaves the nonlinear sample and then calculate the beam profile after it has propagated some distance outside the medium. The information about the effective n_2 is contained in the nature of this profile. In general, the magnitude and sign of the nonlinearity can be determined from the beam profile variation as the sample position is varied about the back focal length of the external lens. The nonlinearity depends on the acceptor-to-donor concentration ratio N_A/N_D, which in turn determines the far-field diffraction pattern. Conversely, measurements of the far-field pattern can be used to calculate N_A/N_D and used as a tool for characterizing different $LiNbO_3$ samples.

2.8.1 Model for Beam Propagation through PR Lithium Niobate

Assume an incident Gaussian beam in the form

$$E_e(x,y,z) = a(z)\exp\left(-\frac{x^2}{w_x^2}\right)\exp\left(-\frac{y^2}{w_y^2}\right) \tag{2.57}$$

Extending 2.56, for an elliptical Gaussian beam, the following relationships holds:

$$\Delta q_x = \Delta z + \frac{q_x^2}{f_{ind_x}}, \quad \Delta q_y = \Delta z + \frac{q_y^2}{f_{ind_y}} \tag{2.58}$$

Since

$$n = n_e + n_2|E_e|^2 \approx n_e - 2n_2a^2(z)\left(\frac{x^2}{w_x^2} + \frac{y^2}{w_y^2}\right) \tag{2.59}$$

where

n_2 is the effective nonlinear refractive index coefficient
n_e is the linear refractive index
E_e is the optical field

We can compute the phase change upon nonlinear propagation through a section Δz of the sample and thereby determine the induced focal length. As expected, these focal lengths are inversely proportional to Δz and can be expressed as

$$f_{ind_x} = \frac{n_e w_x^2}{4n_{2_x}a^2(z)\Delta z}, \quad f_{ind_y} = \frac{n_e w_y^2}{4n_{2_y}a^2(z)\Delta z} \tag{2.60}$$

Substituting (2.60) into (2.58) and taking the limit as $\Delta z \to 0$ we obtain the system of equations

$$\begin{aligned} \frac{dq_x}{dz} &= 1 + \frac{4n_{2_x}a(z)q_x^2}{n_e w_x^2} \\ \frac{dq_y}{dz} &= 1 + \frac{4n_{2_y}a(z)q_y^2}{n_e w_y^2} \end{aligned} \tag{2.61}$$

Using the well-known relationship: $(1/q) = (1/R) + j(\lambda/n_e \pi w^2)$ where R is a radius of Gaussian beam curvature $(1/R) = (1/w)(dw/dz)$, and λ is the wavelength in vacuum, we obtain

$$\begin{aligned} \frac{1}{R_x^2}\frac{dR_x}{dz} &= \frac{n_e^2\pi^2 w_x^4 - \lambda^2 R_x^2}{(n_e \pi w_x^2 R_x)^2} - \frac{4n_{2_x}a^2}{n_e w_x^2} \\ \frac{1}{R_y^2}\frac{dR_y}{dz} &= \frac{n_e^2\pi^2 w_y^4 - \lambda^2 R_y^2}{(n_e \pi w_y^2 R_y)^2} - \frac{4n_{2_y}a^2}{n_e w_y^2} \end{aligned} \tag{2.62}$$

$$\begin{aligned} \frac{d^2 w_x}{dz^2} &= \frac{\lambda^2}{n_e^2\pi^2 w_x^3} - \frac{4n_{2_x}a^2}{n_e w_x} \\ \frac{d^2 w_y}{dz^2} &= \frac{\lambda^2}{n_e^2\pi^2 w_y^3} - \frac{4n_{2_y}a^2}{n_e w_y} \end{aligned} \tag{2.63}$$

Taking into account the relationship for the beam's power, $P = (\pi/2\eta)a^2(z)w_x(z)w_y(z)$ where η is the characteristic impedance of the material, which is conserved, we finally have the system of equations describing the Gaussian beam propagation in a thick $LiNbO_3$ crystal:

$$\begin{aligned} \frac{d^2 w_x}{dz^2} &= \frac{\lambda^2}{n_e^2\pi^2 w_x^3} - \frac{8n_{2_x}P\eta}{\pi n_e w_x^2 w_y} \\ \frac{d^2 w_y}{dz^2} &= \frac{\lambda^2}{n_e^2\pi^2 w_y^3} - \frac{8n_{2_y}P\eta}{\pi n_e w_y^2 w_x} \end{aligned} \tag{2.64}$$

Assuming $n_{2_x} \gg n_{2_y}$ (true for PR lithium niobate) the variation of the widths w_x and w_y of an elliptic Gaussian beam propagating through a thick $LiNbO_3$ sample as shown in the z-scan setup of Figure 2.25 can be modeled by the coupled differential equations:

$$\begin{aligned} \frac{d^2 w_x}{dz^2} &= \frac{\lambda^2}{n_e^2\pi^2 w_x^3} - \frac{8n_2\eta P}{\pi n_e w_x^2 w_y} \\ \frac{d^2 w_y}{dz^2} &= \frac{\lambda^2}{n_e^2\pi^2 w_y^3} \end{aligned} \tag{2.65}$$

The case when $n_{2_x} = n_{2_y}$ has been studied in [41] by employing the q-transformation approach to find the widths of a circular Gaussian beam in a nonlinear medium in the presence of diffraction. Equation 2.65 assume that the nonlinearity is highly inhomogeneous and only affects the

width along the x-axis (which coincides with the c-axis of our crystals) due to the large electron mobility along that axis [25]. The effective n_2 can be written as [41]

$$n_2 \cong -\frac{1}{2} n_e^3 r_{33} \frac{k\alpha\gamma_R N_A}{\mu e \beta N_D} \tag{2.66}$$

where

r_{33} is the electro-optic coefficient
k is the PV constant
α is the absorption coefficient
γ_R is the recombination constant
μ is the mobility
e is the electron charge
β is the thermal generation rate

In the above equation, we have made the assumption $\beta \gg sI$, where s is the ionization cross-section per quantum of light and I is the optical intensity.

2.8.2 z-Scan: Analytical Results, Simulations, and Sample Experiments

In this sub-section, we present analytical and numerical simulation results and compare them with sample experiments using PR $LiNbO_3$. If the Gaussian beam incident on the sample is assumed to have planar wavefronts and waist w_0 (approximately at the back focus of the lens), then

$$w_y^2(z) = w_0^2\left(1+\frac{z^2}{z_{R_y}^2}\right); \quad z_{R_y} = \frac{n_e \pi w_0^2}{\lambda_0} \tag{2.67}$$

For a sample length L assumed to be much larger than the Rayleigh ranges z_{R_y} and z_{R_x} along z for the elliptic beam, the evolution of w_x can be approximated as

$$w_x^2(z) = w_0^2\left(1+\frac{z^2}{z_{R_x}^2}\right); \quad z_{R_x} = \frac{n_e \pi w_0^2}{\lambda_0}\left(1+\frac{4 n_e n_2 \eta \pi P}{\lambda_0^2}\right) \tag{2.68}$$

It is clear that in the x-direction, the beam spread is more than that in the linear diffraction-limited case when $n_2 < 0$ and less when $n_2 > 0$. As seen from relation 2.63 the nonlinearity does not affect the beam width along the y-direction, which leads to elliptic beam cross-section profile at the exit of the crystal and, in general, in the far field.

For more general geometry, where the incident beam does not have a planar wavefront, we have solved Equations 2.65 numerically. Figure 2.26 shows typical z-scan graphs plotted for four different values of power for the initially circularly symmetric Gaussian beam. In the calculations, we have used the following parameters: crystal width $L = 10\,\text{mm}$, lens focal length $f_0 = 10\,\text{cm}$, $\lambda_0 = 514\,\text{nm}$, initial beam width $w_0 = 1.0\,\text{mm}$, $n_e = 2.20$, $n_2 = -1.4 \times 10^{-12}\,\text{m}^2/\text{V}^2$, $P = 1\,\text{mW}$, crystal exit plane to observation plane distance $D = 1\,\text{m}$. A simple explanation of the behavior in the limiting case (s much smaller or larger than f_0) seen in Figure 2.26 can be given by referring to Figure 2.25. When the distance s, lens-to-sample separation, is much smaller than the lens focal length f_0, the incident beam is weakly focused and therefore the beam widths lie close to their linear values leading to semi-linear diffraction-limited propagation. When s is much larger than f_0, the incident beam is weakly diverging and the overall nonlinear effect is small that, in turn, leads to semi-linear diffraction-limited propagation. If $s \sim f_0$, the incident beam is highly focused and therefore the nonlinear effect is large. In this region, as s decreases, the normalized intensity decreases from its linear value, passes through a minimum, and then reaches its maximum before approaching its linear value again. The overall negative slope (between the peak and the valley) of the z-scan confirms the net negative nonlinearity of the sample.

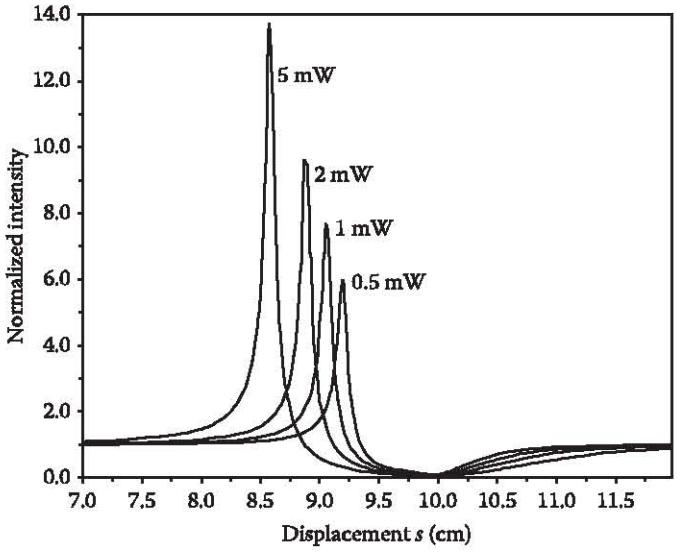

FIGURE 2.26 Typical z-scan graph drawn by solving Equations 2.65 and propagating the Gaussian beam a distance D behind the sample.

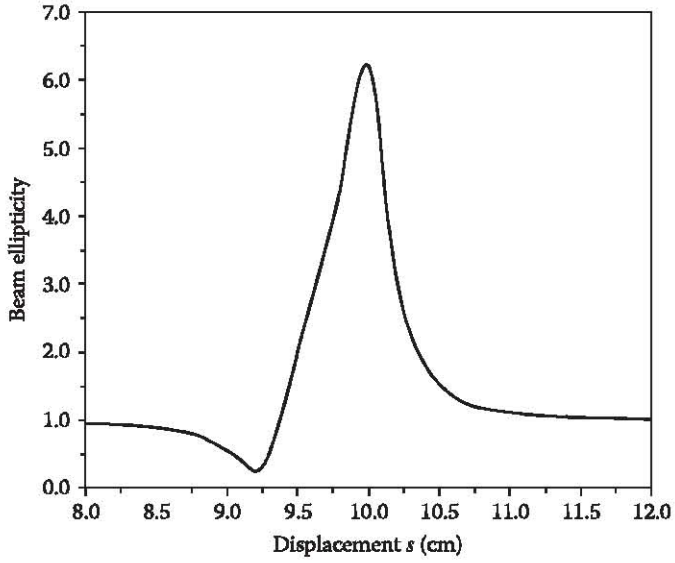

FIGURE 2.27 Plot of ellipticity as function of displacement s for parameters same as in Figure 2.26 but for $P = 0.2$ mW. (From Banerjee, P.P. et al., *J. Opt. Soc. Am. B*, 15, 2446, 1998. With permission.)

Figure 2.27 depicts ellipticity w_x/w_y in the far field versus displacement s drawn for the same set of parameters as that used to draw Figure 2.26, but for $P = 0.2$ mW. We have done a series of sample experiments and compared results. It turns out that the on-axis intensity measurement of far-field patterns may lead to significant errors due to fine structures in the pattern as seen in Figure 2.28 (obtained using a $LiNbO_3$ crystal doped with Fe). We have used this crystal for all experimentation to validate our theory, unless otherwise stated. Possible reasons for this include

1. Interference patterns stemming from single-beam holography [45]
2. Interference patterns from optical misalignment
3. Light diffraction and scattering on crystal defects
4. Interference patterns from nonparallel crystal edges

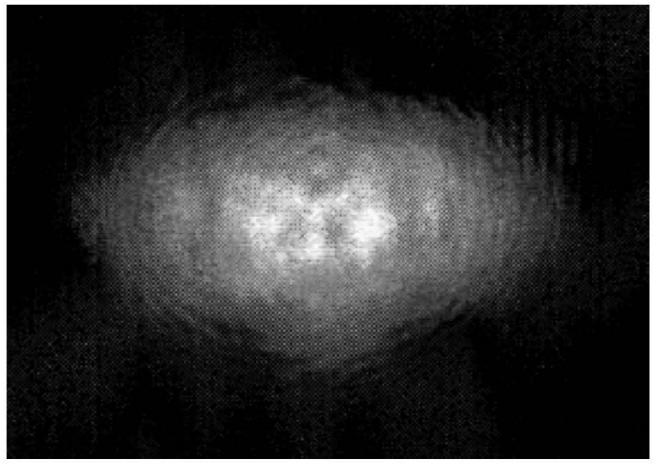

FIGURE 2.28 Typical beam pattern at $D = 0.5\,\text{m}$ for $P = 0.05\,\text{mW}$, $f_0 = 20\,\text{cm}$, and $s = 19.5\,\text{cm}$ for Fe doped $LiNbO_3$ crystal. (From Banerjee, P.P. et al., *J. Opt. Soc. Am. B*, 15, 2446, 1998. With permission.)

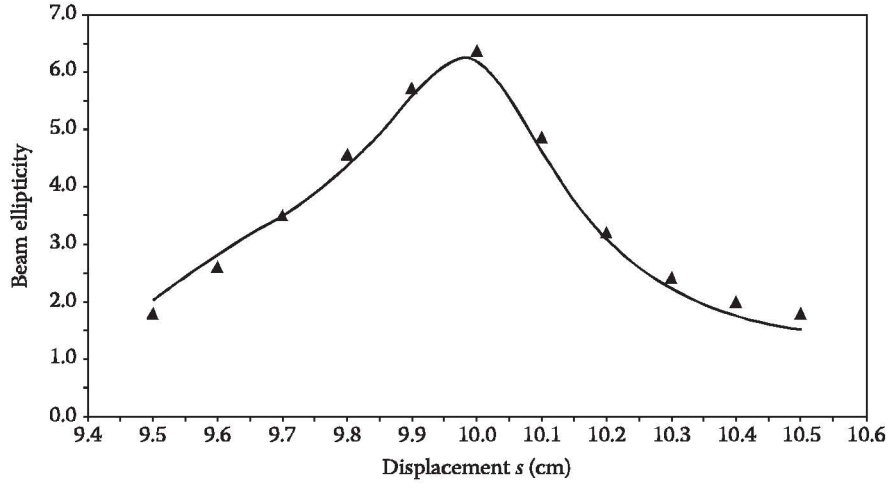

FIGURE 2.29 Experimental (points) and theoretical (line) variation of the beam ellipticity on the observation plane as a function of scan distance. Here, $P = 0.2\,\text{mW}$, $D = 0.5\,\text{m}$, $f_0 = 10\,\text{cm}$. Upon comparison, $n_2 = -1.4 \times 10^{-12}\,\text{m}^2/\text{V}^2$. (From Banerjee, P.P. et al., *J. Opt. Soc. Am. B*, 15, 2446, 1998. With permission.)

Note that the pattern is approximately symmetric (along x and y). This symmetry arises because the refractive index changes that are due to PV (and thermal effects) are symmetric and because there is little contribution from diffusion. Experimental results based on the measurement of ellipticity, as shown in Figure 2.29, show the same trend as the theoretical predictions superposed on the same figure. The ellipticity was calculated from experimental observations by first determining the extent w_x, w_y of the bright or gray region along x and y, respectively, from pictures such as Figure 2.28 and taking the ratio of the two. Note that Figure 2.29 is in fact a blowup of Figure 2.27 over the interval 9.5–10.5 cm. The theoretical graph in Figure 2.29 was drawn after examining the experimental results shown in the same figure and choosing that value n_2 for the analytical graph that minimizes the sum of the differences between the experimental points and the corresponding theoretical data.

As a final note, we would like to point out that each time the crystal was displaced along the longitudinal direction for a fresh z-scan ellipticity measurement, we also made a transverse movement of the crystal in order to make sure that we were starting out from a virgin location in the crystal for each data point. In other words, we always started out from an initially unexposed region of the crystal and exposed it to the incident illumination until steady state was achieved.

In summary, a model for beam propagation through a nonlinear material that takes into account inhomogeneous induced refractive index changes due to the nonlinearity was developed. The theory based on this model can be used to analyze the propagation of Gaussian beams through PR $LiNbO_3$. A focused Gaussian beam of circular cross section incident on the sample emerges as an elliptic Gaussian after interaction in this material. As stated earlier, the simpler P-scan method can be used to evaluate the effective nonlinearities (resulting from the PV effect) of lithium niobate samples doped with different materials such as Fe, Co, Cr, Rh, Mn, etc. The value of the nonlinear coefficient can then be used to determine the acceptor-to-donor ratio of dopants in the PR samples. This method can be used to characterize any optically nonlinear material that has an induced intensity dependent refractive index. We would like to point out that this method is very general and in principle may be applied to any nonlinear electromagnetic material and at any frequency.

PROBLEMS

2.1 Assume a Gaussian beam in air with plane wavefronts and waist w_0 at a distance d_0 from a converging lens of focal length f.
- (a) Using the laws of q-transformation, find the distance behind the lens where the Gaussian beam focuses, i.e., again has plane wavefronts.
- (b) Using the BPM, simulate the propagation of the beam through air and through a lens.
- (c) By setting $d_0 = f$, determine the profile of the beam a distance f behind the lens.
- (d) By setting $d_0 = 2f$, determine the profile of the beam distances f and $2f$ behind the lens.

2.2 A Gaussian beam of width w and having wavefront with a radius of curvature R is normally incident on the interface between air and glass of refractive index n. Find the width and radius of curvature
- (a) Immediately after transmission through the interface
- (b) Immediately upon reflection at the interface

2.3 A Gaussian beam of waist w_0 of wavelength λ is incident on a slice of dielectric material of thickness L with a refractive index $n(x) = n_0 + \Delta n \cos Kx$ with $w_0 \gg 2\pi/K$. Calculate the far-field diffraction pattern of the beam after transmission through the material
- (a) Assuming a thin sample, i.e., $L \ll z_R$ where z_R is the Rayleigh range of the Gaussian beam, and normal incidence
- (b) Assuming a thick sample $L > z_R$ and with $K^2L\lambda \gg 1$, and incidence at Bragg angle given by $\phi_B = \sin^{-1}(K\lambda/4\pi)$

2.4 Use the split-step beam propagation technique to analyze propagation along z of a one-dimensional Gaussian beam of $w_0 = 100\lambda_0$ (λ_0 is the free-space wavelength) incident onto a grating made using a material of quiescent refractive index n_0. The grating has a thickness of $L = 100\lambda_0$ with a refractive index profile $n(x) = n_0 + \Delta n$ sgn $(\cos Kx)$, $K = 2\pi/\Lambda$, $\Lambda = 5\lambda_0$, where sgn denotes the signum function. Assume $n_0 = 1.5$ and $\Delta n = 0.00015$. Calculate the profile at the exit plane of the grating and in the far field. Repeat the problem for the case where the thickness of the grating is $L = 1000\lambda_0$ and characterize the differences between the two cases.

2.5 Analyze the propagation of a Gaussian beam of waist $w_0 = 100\lambda_0$ through a material of thickness $L = 100\lambda_0$ having a refractive index profile $n(x) = n_0 + \alpha(x/w_0)$, $|x| < 5w_0$. Let $n_0 = 1.5$, $\alpha = 0.015$. Determine the far-field intensity profile. You may use analytical techniques and/or the BPM.

2.6 A Gaussian beam of waist $w_0 = 100\lambda_0$ symmetric about $x = 0$ is incident from air onto a nonlinear material slab of thickness $L = 100\lambda_0$ and of refractive index $n(x) = n_0 + n_2 I(x)$, $n_0 = 1$ where $I(x)$ is the intensity of the Gaussian beam. Assume that a knife edge is present

at $z = 0$. Use the split-step method to determine the far-field profile. At $z = 0^-$, assume $n_2 I(0) = 10^{-4}$.

2.7 The paraxial NLS equation can be written as

$$j\frac{\partial u}{\partial z} + \frac{1}{r^{D-1}}\frac{\partial}{\partial r}\left(r^{D-1}\frac{\partial u}{\partial r}\right) + f\left(|u|^2\right)u = 0$$

where D represents the dimension of the problem. For the case $D = 2$ (cylindrical symmetry) and $f(|u|^2) = |u|^2$ (a) use the Hankel transform technique to numerically plot representative beam on-axis amplitudes during propagation all the way to near the self-focusing point for an initial profile $u_0 = 4e^{-r^2/2}$; (b) repeat part (a) for the case when, as in the text, a fixed and adaptive nonparaxiality parameter has been included.

2.8 (a) Plot the on-axis amplitudes as a function of propagation distance for the case of the paraxial NLS equation with cylindrical symmetry but for an initial profile $u_0 = 4e^{-r^2}$. (b) Repeat part (a) for the case when, as in the text, a fixed and adaptive nonparaxiality parameter has been included [22].

2.9 In the paraxial NLS equation

$$j\frac{\partial u}{\partial z} + \frac{1}{r^{D-1}}\frac{\partial}{\partial r}\left(r^{D-1}\frac{\partial u}{\partial r}\right) + f\left(|u|^2\right)u = 0$$

setting $D=3$ implies spherical symmetry. Assume $f(|u|^2) = (|u|^2/(1+\mu|u|^2))$. Use a change of variable $u = r^{-l}v$; $l = 1/2$ to change the radial operator from spherical to cylindrical coordinates. Thereafter, by using a suitable initial condition, sketch typical profiles of the spherically symmetric shapes that are stable during propagation. For hints and details of the Hankel transform to be used, readers are referred to Nehmetallah and Banerjee [46].

2.10 Derive representative z-scan graphs for the case where the (thin) lens to be characterized is a linear lens with a fixed focal length f which is independent of the intensity of the light, but may depend on other parameters such as applied voltage across the sample lens as in an electro-optic lens. In this case, show that the z-derivative of the on-axis intensity is similar to the traditional z-scan signature of a nonlinear induced lens.

2.11 Derive representative z-scan graphs for the case when the sample under test has an induced refractive index as in a diffusion-dominated PR material, and given by $\Delta n \propto \partial I/\partial x$, assuming one transverse dimension. Assume thin sample, for simplicity. Show that the nature of the z-scan graph is an even function of the displacement from the back focal plane of the external lens. For hints and details, readers are referred to Noginov et al. [47].

2.12 If the induced refractive index of a material is proportional to the gradient of the intensity, show how this effect may be used in image processing applications such as edge enhancement of an image. For hints, readers are referred to Banerjee et al. [48].

REFERENCES

1. P.P. Banerjee and T.C. Poon, *Principles of Applied Optics*, CRC Press, Boca Raton, FL, 1991.
2. G.P. Agrawal, *Nonlinear Fiber Optics*, Academic, London, 1989.
3. R.H. Hardin and F.D. Tappert, Applications of the split-step Fourier method to the numerical solution of nonlinear and variable coefficient wave equations, *SIAM* 15, 423, 1973.
4. A. Korpel, *Acousto-Optics*, 2nd edn., Dekker, Amsterdam, 1997.
5. C. Venzke, A. Korpel, and D. Mehrl, Improved space-marching algorithm for strong acousto-optic interaction of arbitrary fields, *Appl. Opt.* 31, 656–654, 1992.

6. P.P. Banerjee and C.-W. Tarn, A Fourier transform approach to acoustooptic interactions in the presence of propagational diffraction, *Acustica* 74, 181–191, 1991.
7. P.P. Banerjee, *Nonlinear Optics*, Dekker, New York, 2004.
8. G. Fibich and A. Gaeta, Critical power for self-focusing in bulk optical media and in hollow waveguides, *Opt. Lett.* 25, 335–337, 2000.
9. V.E. Zakharov and D. Shabat, Exact theory of two-dimensional self-focusing and one-dimensional self-modulation of waves in nonlinear media, *Sov. Phys. JETP* 34, 62–69, 1972.
10. G. Nehmetallah and P.P. Banerjee, Study of soliton stabilization in ($D=1$) dimensions using novel analytical and numerical techniques, in *Nonlinear Optics and Applications*, H.A. Abdeldayem and D.O. Frazier, eds., Research Signpost, Trivandrum, India, 2007.
11. A. Korpel, K.E. Lonngren, P.P. Banerjee, H.K. Sim, and M.R. Chatterjee, Split-step-type angular plane-wave spectrum method for the study of self-refractive effects in nonlinear wave propagation, *J. Opt. Soc. Am. B* 3, 885–890, 1986.
12. H.K. Sim, A. Korpel, K.E. Lonngren, and P.P. Banerjee, Simulation of two-dimensional nonlinear envelope pulse dynamics by a two-step spatiotemporal angular spectrum method, *J. Opt. Soc. Am. B* 5, 1900–1909, 1988.
13. G. Fibich, Small beam nonparaxiality arrests self-focusing of optical beams, *Phys. Rev. Lett.* 76, 4356–4359, 1996.
14. D.W. McLaughlin, G.C. Papanicolaou, C. Sulem, and P. L. Sulem, The focusing singularity of the cubic Schrödinger equation, *Phys. Rev. A* 34, 1200–1210, 1986.
15. M.I. Weinstein, Nonlinear Schrodinger equation and sharp interpolation estimates, *Comm. Math. Phys.* 87, 567–576, 1983.
16. R.T. Glassey, On the blowing up of solutions to the Cauchy problem for nonlinear Schrodinger equations, *J. Math Phys.* 18, 1794–1797, 1977.
17. P. Sulem, C. Sulem, and A. Patera, Numerical solution of the singular solutions to the 2-dimensional cubic Schrodinger equation, *Commun. Pure Appl. Math.* 37, 755–778, 1984.
18. G. Fibich and G.C. Papanicolaou, Self-focusing in the perturbed and unperturbed nonlinear Schrodinger equation in critical dimension, *SIAM J. Appl. Math.* 60, 183–240, 1999.
19. A.E. Siegman, Quasi-fast Hankel transform, *Opt. Lett.*, 1, 13–15, 1977.
20. L.C. Andrews and B.K. Shivamoggi, *Integral Transforms for Engineers*, SPIE, Bellingham, WA, 1998.
21. L. Yu, M. Huang, M. Chen, W. Chen, W. Huang, and Z. Zhu, Quasi-discrete Hankel transform, *Opt. Lett.* 23, 409–411, 1998.
22. P.P. Banerjee, G. Nehmetallah, and M.R. Chatterjee, Numerical modeling of cylindrically symmetric nonlinear self-focusing using an adaptive fast Hankel split-step method, *Opt. Commun.* 249, 293–300, 2005.
23. G. Fibich and B. Ilan, Discretization effects in the nonlinear Schrodinger equation, *Appl. Num. Math.* 44, 63–75, 2003.
24. S. Chi and Q. Guo, Vector theory of self-focusing of an optical beam in Kerr media, *Opt. Lett.* 20, 1598–1600, 1995.
25. P. Yeh, *Introduction to Photorefractive Nonlinear Optics*, Wiley, New York, 1993.
26. J. Feinberg, Asymmetric self-defocusing of an optical beam from the photorefractive effect, *J. Opt. Soc. Am.* 72, 46–51, 1982.
27. J.J. Liu, P.P. Banerjee, and Q.W. Song, Role of diffusive, photovoltaic, and thermal effects in beam fanning in $LiNbO_3$, *J. Opt. Soc. Am. B* 11, 1688–1693, 1994.
28. V.V. Voronov, I.R. Dorosh, Yu.S. Kuz'minov, and N.V. Tkachenko, Photoinduced light scattering in cerium-doped barium strontium niobate crystals, *Sov. J. Quantum Electron.* 10, 1346–1349, 1980.
29. P.P. Banerjee and R.M. Misra, Dependence of photorefractive beam fanning on beam parameters, *Opt. Commun.* 100, 166–172, 1993.
30. P.P. Banerjee and J.-J. Liu, Perturbational analysis of steady state and transient beam fanning in thin and thick photorefractive media, *J. Opt. Soc. Am. B* 10, 1417–1423, 1993.
31. M. Segev, Y. Ophir, and B. Fischer, Nonlinear mutli two-wave mixing. The fanning process and its bleaching in photorefractive media, *Opt. Commun.* 77, 265–274, 1990.
32. G.A. Swartzlander and A.E. Kaplan, Self-deflection of laser beams in a thin nonlinear film, *J. Opt. Soc. Am. B* 5, 765–768, 1988.
33. M. Abramowitz and I.A. Stegun, *Handbook of Mathematical Functions*, Dover, New York, 1970.
34. K. Ratnam and P.P. Banerjee, Nonlinear theory of two-beam coupling in a photorefractive material, *Opt. Commun.* 107, 522–530, 1994.

35. M. Cronin-Golomb and A. Yariv, Optical limiter using photorefractive nonlinearities, *J. Appl. Phys.* 57, 4906–4910, 1985.
36. S.E. Bialkowski, Application of $BaTiO_3$ beam-fanning optical limiter as an adaptive spatial filter for signal enhancement in pulsed infrared laser-excited photothermal spectroscopy, *Opt. Lett.* 14, 1020–1022, 1989.
37. S. Guha, Validity of the paraxial approximation in the focal region of a small *f*-number lens, *Opt. Lett.* 26, 1598–1600, 2001.
38. J.-J. Liu and P.P. Banerjee, Role of diffusive, photovoltaic and thermal fields in beam fanning in LiNbO3, *J. Opt. Soc. Am. B* 11, 1688–1693, 1994.
39. M.A. Saleh, Self-pumped Gaussian beam coupling and stimulated backscatter due to reflection gratings in a photorefractive material, PhD dissertation, University of Dayton, Dayton, OH, 2007.
40. G. Cook, C.J. Finman, and D.C. Jones, Photovoltaic contribution to cunterpropagating two-beam coupling in photorefractive lithium niobate, *Opt. Commun.* 192, 393–398, 2001.
41. P.P. Banerjee, R.M. Misra, and M. Maghraoui, Theoretical and experimental studies of propagation of beams through a finite sample of a cubically nonlinear material, *JOSA B* 8, 1072–1080, 1991.
42. M. Sheik-Bahae, A.A. Said, and E.W. Van Stryland, High-sensitivity, single-beam n_2 measurements, *Opt. Lett.* 14, 955–957, 1989.
43. Q.W. Song, C.-P. Zhang, and P.J. Talbot, Anisotropic light-induced scattering and "position dispersion" in $KNbO_3$:Fe crystal, *Opt. Commun.* 98, 269–273, 1993.
44. P.P. Banerjee, A. Danilieko, T. Hudson, and D. McMillen, P-scan analysis of induced inhomogeneous optical nonlinearities, *J. Opt. Soc. Am. B* 15, 2446–2456, 1998.
45. N. Kukhtarev, G. Dovgalenko, G. Duree, G. Salamo, E. Sharp, B. Wechler, and M. Klein, Single beam polarization holographic grating recording, *Phys. Rev. Lett.* 71, 4330–4332, 1993.
46. G. Nehmetallah and P.P. Banerjee, Numerical modeling of spatio-temporal solitons using an adaptive spherical Forurier Bessel split-step method, *Opt. Commun.* 257, 197–205, 2006.
47. M. Noginov, S.W. Helzer, G.B. Loutts, P.P. Banerjee, M. Morrisey, and Y. Kim, Study of photorefraction response and diffraction efficiency in Mn:YAlO3 crystals, *J. Opt. Soc. Am. B* 20, 1233–1241, 2003.
48. P.P. Banerjee, H.-L. Yu, D. Gregory, and N. Kukhtarev, Phase conjugation, edge detection and image broadcasting using two-beam coupling in photorefractive potassium niobate, *Opt. Photonics Tech. Lett.* 28, 89–92, 1996.